Universität Hamburg
DER FORSCHUNG | DER LEHRE | DER BILDUNG

FAKULTÄT
FÜR MATHEMATIK, INFORMATIK
UND NATURWISSENSCHAFTEN

Master's Thesis

It st·ar·ts -

Modelling the Transfer of Solar Radiation in Planetary Atmospheres

Jon Petersen

jon.petersen@studium.uni-hamburg.de
Course: M. Sc. Meteorologie
Matr.-No.: 6939930

Primary supervisor: Prof. Stefan Buehler (UHH)
Secondary supervisor: Dr. Manfred Brath (UHH)

Submission: December 2022

Modelling the Transfer of Solar Radiation through the Atmosphere

Abstract

An external stellar source is introduced to the Atmospheric Radiative Transfer Simulator (ARTS). In principle, ARTS can simulate multiple host stars for a user-defined planet, however, the Earth-Sun system is mainly investigated. Previously, ARTS was designed for the millimetre and sub-millimetre spectral range, but this extension allows for simulations in the shortwave down to the ultra-violet wavelengths. This enables the usage of ARTS for satellite retrievals in the visible and near-infrared range and a consistent integration of longwave and shortwave radiative transfer into other models as the radiative-convective equilibrium model KONRAD. With the extension, ARTS may also be used as a reference model to develop radiative forcing parametrizations for climate models in the shortwave regime.

The radiation transport simulated by the ARTS internal `iyClearsky` solver is compared to the integrated DISORT solver, and it is found that the scattering of the radiation reflected from the surface should not be negligible. This is because it otherwise produces errors of at least 30 % in the diffuse field, which accounts for 7.7 % of the total downward flux at the surface and a solar zenith angle of 0 degrees. The single scattering approximation produces errors of about 2.3 % for solar zenith angles of 0 degrees. This error grows to 14.4 % for a solar zenith angle of 60 degrees.

Using DISORT as a solver for the simulations results in meaningful and coherent simulations of shortwave fluxes. These fluxes were compared using reference simulations by LBLRTM (Line-By-Line Radiative Transfer Model) and RRTMG (Rapid Radiative Transfer Model - General Circulation Models Applications) of the present-day experiment of the Radiative Transfer Model Intercomparison Project (RFMIP). ARTS was found to be in better agreement with the physically more accurate LBLRTM model compared to RRTMG. With adjustments for the solar position and total solar irradiance, to compensate for the different geometries between the models, it can determine fluxes at the top of the atmosphere (TOA) to on average $0.4\,\mathrm{mW\,m^{-2}}$ accuracy of target total solar irradiance. The difference between ARTS and LBLRTM is $0.75 \pm 0.40\,\mathrm{W\,m^{-2}}$ in the downward flux at the surface and $0.50 \pm 0.36\,\mathrm{W\,m^{-2}}$ in the upward flux at TOA. It is found that the differences between ARTS and LBLRTM increase linearly with the effective path length through the atmosphere. Differences are suspected in a too weak water vapour absorption due to different continua versions and a too high Rayleigh scattering coefficient, leading to stronger scattering than found in LBLRTM. The absorption by the newly integrated ozone absorption cross sections provides similar absorption as in LBLRTM.

Zusammenfassung

Der Atmospheric Radiative Transfer Simulator (ARTS) wird um eine externe, stellare Quelle erweitert. Im Prinzip kann ARTS mehrere Wirtsterne für einen benutzerdefinierten Planeten simulieren, jedoch wird hauptsächlich das Erde-Sonne-System untersucht. Bisher war ARTS nur für den Millimeter- und Submillimeter-Spektralbereich ausgelegt. Diese Erweiterung bietet nun die Möglichkeit, Simulationen im kurzwelligen Spektralbereich bis hinunter zum Ultraviolett durchzuführen. Somit bietet ARTS Anwendungen für Satellitenretrievals im sichtbaren und nahen Infrarotbereich, eine konsistente Integration in andere Modelle wie das radiative-convective equilibrium model KONRAD, sowie den Einsatz als Referenzmodell für die Entwicklung von Parametrisierungen des kurzwelligen Strahlungsantriebs für Klimamodelle.

Die simulierte Strahlung vom ARTS-internen `iyClearsky`-Solver wurde mit dem in ARTS integrierten DISORT-Solver verglichen. Es wurde festgestellt, dass die Streuung der von der Oberfläche reflektierten Strahlung einbezogen werden sollte. Andernfalls kommt es zu Fehlern von mindestens 30 % des diffusen Feldes, was 7,7 % des gesamten abwärts gerichteten Flusses an der Oberfläche und einem solaren Zenitwinkel von 0 Grad entspricht. Die Vereinfachung durch Einfachstreuung führt zu Fehlern von etwa 2,3 % für einen solaren Zenitwinkel von 0 Grad. Dieser Fehler wächst auf 14,4 % für einen solaren Zenitwinkel von 60 Grad an.

Die Verwendung von DISORT als Strahlungssolver führt zu aussagekräftigen und kohärenten Simulationen der kurzwelligen Flüsse. Diese Flüsse wurden mit Referenzsimulationen des LBLRTM (Line-By-Line Radiative Transfer Model) und RRTMG (Rapid Radiative Transfer Model - General Circulation Models Applications) des 'present-day' Experiments des Radiative Transfer Model Intercomparison Projects (RFMIP) verglichen. Es wurde festgestellt, dass ARTS besser mit dem physikalisch genaueren LBLRTM-Modell übereinstimmt als mit RRTMG. Mit Anpassungen der solar Konstanten und der Position der Sonne, zur Kompensation der unterschiedlichen Geometrien der Modelle, kann ARTS die Flüsse am Oberrand der Atmosphäre (TOA) mit einer durchschnittlichen Genauigkeit von 0,4 $\mathrm{mW\,m^{-2}}$ der gewünschten Solareinstrahlung bestimmen. Der Unterschied zwischen ARTS und LBLRTM beträgt $0,75 \pm 0,40\,\mathrm{W\,m^{-2}}$ im Abwärtsfluss an der Oberfläche und $0,50 \pm 0,36\,\mathrm{W\,m^{-2}}$ im Aufwärtsfluss am TOA. Die Unterschiede zwischen ARTS und LBLRTM nehmen linear mit der effektiven Pfadlänge durch die Atmosphäre zu. Es wird vermutet, dass die Unterschiede durch eine zu schwache Wasserdampfabsorption verursacht werden. Dies ist auf unterschiedliche Kontinua-Versionen zurückzuführen. Zudem scheint ARTS einen größeren Rayleigh-Streukoeffizienten zu

berechnen, was im Vergleich zu LBLRTM zu stärkerer Streuung führt. Die Absorption durch die neu integrierten Ozon Absorptionquerschnitte ist übereinstimmend mit der Absorption in LBLRTM.

Contents

1 Introduction

The Atmospheric Radiative Transfer Simulator, ARTS is a well-established radiative transfer model (RTM) in the longwave community with various application possibilities for different instruments (Buehler et al. [2005], Eriksson et al. [2011], artswebpage). An RTM simulates the electromagnetic spectrum at a given position and viewing angle for user-defined atmospheres, e.g. what a given satellite would measure based on position, sensor and atmospheric state. This is used in satellite retrievals. So far, ARTS had the limitation that it was not possible to do simulations with a solar source. Thus, it was not suited for any application in the shortwave regime. As the title 'It starts' of this thesis suggests, the aim of my work is to extend ARTS to the shortwave regime by including stars such as the Sun as an external source. Now we start simulating stars in ARTS. Therefore 'It starts'! Generally, ARTS can simulate different planets with different systems of stars, but this study will focus on the Earth and its star the Sun because we have the most knowledge and data to compare against and a more intuitive understanding of the system.

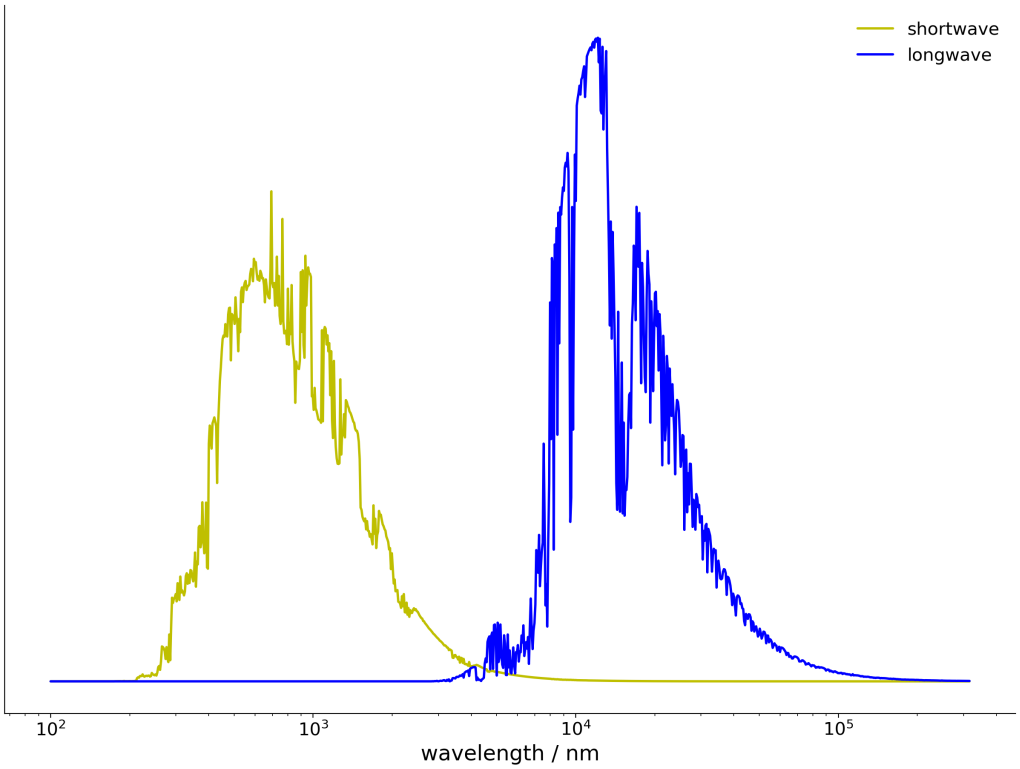

Figure 1.1: Conceptual illustration for shortwave (yellow) and longwave (blue) simulations using ARTS.

Figure 1.1 shows an ARTS simulation of the outgoing longwave radiation (blue line) as an example of the currently possible wavelength domain. The yellow line shows the addition of the shortwave regime as introduced in the context of this thesis. It becomes evident that due to the ability to simulate in this spectral regime, ARTS gains completely new application possibilities, which are influenced by solar radiation and were therefore impossible to simulate before.

For instance, new application possibilities are satellite retrievals, which can now also be performed in the shortwave range. This was not possible with the old ARTS or only partially in the near-infrared. Previously, it was necessary to estimate the extent to which one could simulate in the near-infrared and the associated error. Now the model is consistent over all meteorologically important wavelengths and all channels of conventional weather satellites can be used for the retrievals. Thus, more accurate results can be obtained. This thesis deals with clear sky conditions but a long-term goal is to extend simulations to cloudy conditions. Then complete satellite scenes could be simulated.

Another application of ARTS is that it is integrated into other models, such as the radiative-convective equilibrium model Konrad [Kluft et al., 2020], in order to calculate the radiation balance therein. Until now, ARTS could only be used for the longwave part, and other models had to handle the shortwave part. My extensions allow these models to use consistent radiation simulations from ARTS alone.

In addition, ARTS is, among other models, used as a reference for radiative forcing in the Coupled Model Intercomparison Project (CMIP) [Taylor et al., 2012], which provides the basis for the IPCC (The Intergovernmental Panel on Climate Change) reports [Houghton et al., 1990]. Reference models for radiative transfer are known for their high accuracy compared to laboratory experiments. Yet their high spectral resolution excludes their use in climate models since it would be computationally too inefficient. Essentially, the entire shortwave and longwave spectra must be parameterized by several wavelength intervals to allow acceptable run times in global climate models [Pincus et al., 2015]. Therefore, the better the references are, the more accurate parameterizations can be developed. For comparability between RTMs, the RFMIP (Radiative Forcing Model Intercomparison Project) was initiated by Pincus et al. [2016]. There, results for defined atmospheric conditions and compositions, representing different conditions in the past, present-day, and possible future scenarios, are compared. However, this thesis aims not to provide another reference in the context of the RFMIP but rather to evaluate the shortwave part of ARTS using the results of other RTMs and to identify possible weaknesses.

The remainder of this thesis is structured as follows: First Chapter 2 describes the data and external software used. In Chapter 3 the basic principles of radiation are introduced, and the radiative transfer equation is defined. Based on this, the ARTS solver `iyClearsky` and DISORT [Stamnes et al., 2000] with the respective simplification and approximations are explained. Finally, the conceptual separation between the longwave

and the shortwave regime, which can be seen in Figure 1.1, is described and explained in more detail. Chapter 4 first examines the dependencies of various quantities, such as the spectral grid (Sec. 4.3) and the reference solar spectra (Sec. 4.4) on the shortwave fluxes. Then the two solvers `iyClearsky` and DISORT are compared in Section 4.2. Subsequently, first findings, insights and conclusions of simulations in the shortwave are collected and analyzed. In Chapter 5 the RFMIP reference cases' simulations are shown and compared to other state-of-the-art RTMs. All results and insight gained from simulations in the shortwave regime are then summarized and concluded in Chapter 6, and perspective is given on what can be improved or investigated in more detail (see Ch. 7).

2 Data and Software

This chapter describes the software and data sets used in this thesis.

2.1 Software

2.1.1 ARTS

Since this thesis is about the expansion of ARTS to the short wavelength region of the spectrum, it is obvious that ARTS is part of the software used. Currently ARTS is a radiative transfer model for millimeter and sub-millimeter wavelengths. Without loss of generality it is used for different sensors in different applications. As ARTS is constantly changing and therefore, in order to create consistency between the results, all calculations and analyses were made with the ARTS version of the git id: 1128880 (https://github.com/atmtools/arts/tree/1128880a26217f43f65140b4739ff89b3927a98c).

2.1.2 DISORT

DISORT (DIScrete Ordinate Radiative Transfer) [Stamnes et al., 2000] is a 1D scalar, plane-parallel radiative transfer solver, which accounts for multiple scattering, internal Planck sources, and reflection from a lower boundary and is applicable from the ultraviolet to the radar band of the electromagnetic spectrum. DISORT efficiently calculates accurate fluxes and intensities at any user-specified angle and location within the given atmosphere, and has been used in a variety of software tools and packages. All simulation in this study uses the cDISORT (Version 2.1.2) implementation, which is rewritten in C from Fortran (Version 2.1).

2.2 Data

2.2.1 Solar Spectrum

The Solar Irradiance Climate Data Record [Coddington et al., 2015] provides five reference spectra indicative of quiet, low, moderate and high solar activity levels and the Maunder Minimum. They give the energy input to the top of the Earth's atmosphere at a standard (invariant) distance of one astronomical unit (1 au) from the sun. Values of solar spectral irradiance are provided in 99885 bins of equal 1 nm width, from 115.5 nm

to 99,999.5 nm, in units of $\mathrm{W\,m^{-2}\,nm^{-1}}$. The total (spectrally integrated) solar irradiance (TSI) is the rate of transport of total radiative energy per unit area that the sun provides at the top of Earth's atmosphere. It is known as the solar constant and has a value of about $1361\,\mathrm{W\,m^{-2}}$. The shape of the spectrum is similar to the spectrum of a blackbody with a temperature of 5,770 K which roughly corresponds to the temperature of the emitting layer of the sun from which 99 % of the radiation originates [Coddington et al., 2016].

2.2.2 Ozone Cross-sections

ARTS comes with a collection of line and cross-section data [artscat] where most of the absorption data originates from the HITRAN spectroscopic database [Rothman et al., 2003] (Version HITRAN2016). However, there is no line data for ozone in the visible (VIS) and ultraviolet (UV) range, which plays a significant role there. To cover this, ozone cross-sections measured by Gorshelev et al. [2014] and Serdyuchenko et al. [2014] are used. The cross-sections ranges from 213 nm to 1100 nm with a spectral resolution of 0.02–0.06 nm in the UV–VIS and 0.12–0.24 nm in the infrared (IR) and is interpolated on a equidistant grid of 1 nm. They are given for eleven temperatures ranging from 193 K to 293 K in steps of 10 K. The absolute accuracy is better than three percent for most parts of the spectral region and wavelength calibration accuracy is better than 0.005 nm.

2.2.3 FASCOD Atmosphere

There is also a collection of atmospheric profiles and auxiliary datasets for ARTS [artsxml]. One of these datasets are the FASCOD atmospheres, which provide 1D profiles of the volume mixing ratios from surface up to 95 km altitude for 28 major and trace gases as well as temperature and pressure profiles [Anderson et al., 1986].

2.2.4 RFMIP

The Radiative Forcing Model Intercomparison Project seeks to answer the question how the Earth systems responds to different forcings. It provides 18 sets (or referred to as experiments) of atmospheric conditions from preindustrial levels over present day (interpreted as the year 2014) to predicted values for the future and with different gas concentrations (for example scaling CO_2 concentrations) to evaluate the influence of atmospheric conditions on the radiative forcing. Each experiment consists of 100 sites spread around the globe covering a variety of different atmospheric states, solar zenith angles and gas concentration profiles to characterize global and regional effects. To get a representative global mean, the fluxes of all sites can be combined with the respective weighting factor. The project is described in more detail in Pincus et al. [2016] and results of the project can be found in Pincus et al. [2020]. For this work, results are compared against simulations of LBLRTM [Clough et al., 2005] and RRTMG [Mlawer et al., 1997].

3 Theoretical Background

This chapter will introduce the basic radiation units with an overview of the different spectral ranges and some essential concepts in the beginning. Then, the radiative transfer equation, which is the foundation of all radiation transfer, is defined and its terms are described with emphasis on the short wavelength regime. Thereafter, the solution approach is described and which assumptions are included in different solvers used in this thesis. At the end of this chapter, the introduced concepts are implemented in the first simulation and, based on this, the concept of separation of the short- and longwave regimes is described and analyzed with respect to the terms of the radiative transfer equation.

3.1 Pencils of radiation

The fundamental element for radiative transfer in planetary atmospheres is the 'pencil beam', which can be understood as a direct beam of photons in a given direction and at a given frequency ν or wavelength λ (the two quantities are interchangeable with the relationship $\nu = c_0/\lambda$ with c_0 being the speed of light in a vacuum). To describe it, one needs to know how much radiant energy dE_λ passes through a unit area dA in a time interval dt with a specific wavelength interval $d\lambda$ in a direction distended by an interval of solid angle $d\Omega$ oriented by the angle of incidence θ to the area's normal:

$$I_\lambda = \frac{dE_\lambda}{cos\theta \; d\Omega \; d\lambda \; dt \; dA}. \tag{3.1}$$

This quantity I_λ is called intensity or spectral radiance and has units of $\mathrm{J\,m^{-2}\,m^{-1}\,sr^{-1}\,s^{-1}}$ or $\mathrm{W\,m^{-2}\,m^{-1}\,sr^{-1}}$, which is more commonly used. The $cos\theta$ term comes from the fact when the direction of propagation of the radiation is normal to the unit area the most energy is transported. With larger angle of incidence, less energy is transported through the surface, because the projected area becomes smaller.

Since this thesis is about the introduction of shortwave radiation in ARTS, the spectral unit wavelength $d\lambda$ is used as it is the common unit in the shortwave regime. The shortwave regime is also called solar radiation because most of the solar energy density is located there. It is further divided into the ultraviolet (UV), visible (VIS), and near-infrared (IR) spectral bands and there the wavelength is usually expressed in nanometers ($1\,\mathrm{nm} = 10^{-9}\,\mathrm{m}$). This is the region of interest. An overview of all spectral bands is given in Figure 3.1. Towards longer wavelengths the thermal infrared, microwave and radio

wave (sub-millimetre) regions are located. Until now, ARTS was only able to simulate radiation in these regions. For completeness, the gamma-ray, X-ray, and the shorter-wavelength (extreme/ far) UV regions are also shown. These are mostly of interest for astrophysics and processes in the upper atmosphere but are not discussed in this thesis.

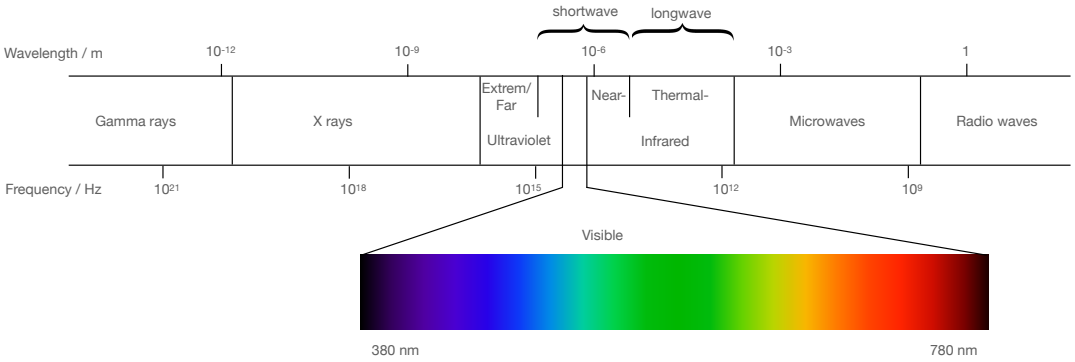

Figure 3.1: Visualisation of the different spectral regimes with their corresponding wavelengths and frequencies.

Integrating the intensity over all wavelengths gives the broadband intensity or radiance:

$$I = \int_0^\infty I_\lambda \, d\lambda. \tag{3.2}$$

This quantity is still directed but has no spectral information.

If the integration is performed not spectrally but over the entire hemispheric solid angle of the normal component of I_λ, one obtains the spectral irradiance:

$$F_\lambda = \int_\Omega I_\lambda \, cos\theta \, d\Omega. \tag{3.3}$$

This quantity contains spectral information but combines radiation propagating down- or upward. We speak of downward irradiances when integrating over the upper hemisphere, as it is the radiation propagating downward and vice versa. In ARTS, the hemispheres are separated by surfaces of constant geopotential. As ARTS internally uses frequency ν as its base unit the spectral irradiance must be transformed. Since the total energy must be conserved ($F(\lambda) = F(\nu)$), we can formulate the relationship between the

spectrally resolved quantities as follows:

$$F_\lambda = -(c/\nu^2)F_\nu. \tag{3.4}$$

ARTS uses frequency because it does not change in a medium with different refractive index n, where the wavelength does change to account for the change in the speed of light c ($\nu = n \cdot c_0/\lambda_0 = c/\lambda$). Furthermore, it is attractive because the energy of photons is given by $h\nu$ with the Planck constant h. Hence increasing ν is associated with photons of higher energy.

Integrating in the spectral and spacial dimensions, we receive the broadband irradiance. One can recognise that F is a flux of energy, i.e., it has units of $\mathrm{W\,m^{-2}}$. Hence the choice of the symbol F. It is for example used to describe the total energy input from the Sun at the top of the atmosphere (TOA), the so called solar constant with $1360.8 \pm 0.5\,\mathrm{W\,m^{-2}}$ [Thomas and Stamnes, 2002].

3.2 Radiative Transfer Equation

In this section the radiative transfer equation (RTE) is introduced. It is the foundation of all radiative transfer. It describes how radiation is modified and distributed as it propagates through a medium. The RTE is defined as:

$$\frac{dI_\lambda}{ds} = -k\ I_\lambda + \alpha\ I_B(T) + \sigma \int_{4\pi} P\ I_\lambda\ d\Omega. \tag{3.5}$$

In the following, the 3 terms will be described and approximations to simplify the solving of the RTE are introduced.

3.2.1 Extinction

The first term in the RTE is the extinction term. It describes the extinction of radiant energy passing through the matter by absorption and scattering. The extinction coefficient k is the sum of the absorption coefficient α as absorption leads to attenuation of radiation and the scattering coefficient σ because scattering causes energy to be redirected from this direction into another (of cause it is a source for the direction it got redirected in - this is the third term (see Sec. 3.2.3)). These are two very different processes and are described separately in the following sections:

Absorption

The absorption coefficient α, which is highly dependent on wavelength, is calculated based on a compilation of spectroscopic parameters found in the ARTS catalogue data [artscat]. Most data originates from the HITRAN spectroscopic database [Rothman et al.,

2003]. The catalogue covers all important absorbers such as water vapour (H_2O), oxygen (O_2), carbon dioxide (CO_2) and methane (CH_4) [Liou, 2002a, Vardavas et al., 2011] in the shortwave regime. Thus, the existing longwave model for absorption can be easily extended to the shortwave regime. However, one piece is missing, as HITRAN does not cover important ozone (O3) absorption bands in the UV-VIS. To fill this gap, ozone cross-sections from Gorshelev et al. [2014], Serdyuchenko et al. [2014] (described in Sec. 2.2.2) are taken, and fit parameters are calculated to match the ARTS internal format for absorption. For this, a polynomial model is used as described in Buehler et al. [2022].

Scattering

For scattering, the decisive factor is the ratio of the size of the scattering object to the wavelength. This can be expressed by the scale parameter

$$x = \frac{2\pi r}{\lambda}, \tag{3.6}$$

where r is the representative radius of the scattering object. In clear-sky cases - atmospheres without rain, cloud droplets, and aerosols - scattering is negligible in the IR, as the wavelength is orders of magnitude larger than the molecules in the air. In the shortwave regime, the wavelength is of similar size as but still larger than the air molecules, and the scale parameter approaches a value of $r \geqslant 0.002$, where Rayleigh scattering is becoming important [Petty, 2006]. Other scattering domains are Mie and optical scattering, which are essential when the wavelength is about the same size as or smaller than the scattering object (e.g. rain droplets in the infrared or general reflection on a mirror), respectively.

The scattering coefficient for Rayleigh scattering is in itself highly dependent on the wavelength. As scattering theory is quite complex, I use an empirical fit for the Rayleigh scattering coefficient described by Thomas and Stamnes [2002] based on numerical results of Bates [1984]. The Rayleigh scattering cross-section for air according to this fit is:

$$\sigma_{ray,xsec} = 10^{-16}\lambda^{-4}\sum_{i=0}^{3} a_i\lambda^{-2i} \quad \left[\mathrm{cm}^2\right] \tag{3.7}$$

with the wavelength λ given in nm and the coefficients being:

$$\begin{aligned} a_0 &= 3.9729066 \\ a_1 &= 4.6547659 \cdot 10^4 \\ a_2 &= 4.5055995 \cdot 10^8 \\ a_3 &= 2.3229848 \cdot 10^{13}\,. \end{aligned}$$

According to Thomas and Stamnes [2002], the formula is accurate to 0.3% for wavelengths between 205 nm and 1050 nm. With the Rayleigh scattering cross-section, one

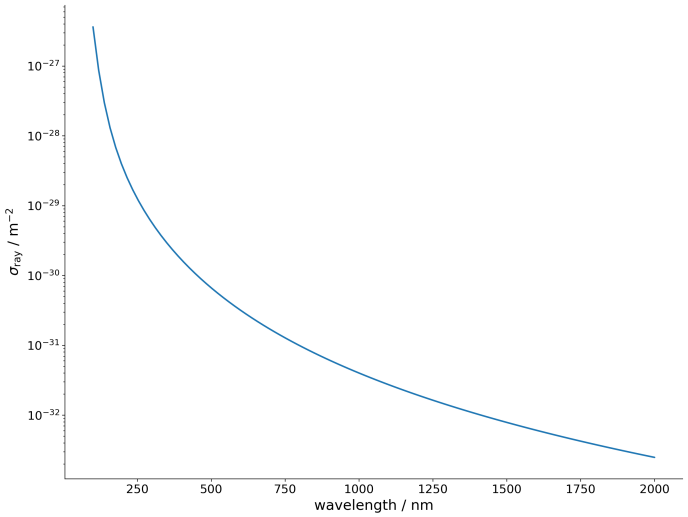

Figure 3.2: Empirical fit for the Rayleigh scattering cross-section.

can calculate the Rayleigh scattering coefficient with

$$\sigma = N\sigma_{ray,xsec} = \frac{p}{Tk_b}\sigma_{ray,xsec}, \tag{3.8}$$

where N denotes the number density, p pressure, T temperature and k_B the Boltzmann constant. The Rayleigh scattering coefficient determines the strength of scattering for different wavelength and atmospheric properties.

Figure 3.2 shows how the empirical fit for the Rayleigh scattering cross-section (see Eqn. 3.7) is decreasing with wavelength. This strong decrease with wavelength is the reason for the blue colour of our sky because blue light with about half of the wavelength as red light is scattered about 16 times as effectively. Thus, the sky appears blue during the day.

A way to quantify attenuation of the radiation is with the opacity or optical depth/optical thickness. The optical depth τ is dimensionless, and is in particular not a length, though it is monotonically increasing with the optical path length, and approaches zero as the path length approaches zero. When the optical depth is 1, the radiation is attenuated by a factor of $1/e$. The optical depth of the entire clear-sky atmosphere at a given wavelength may be calculated from the absorption and scattering coefficient in the form [Liou, 2002a]:

$$\tau(s_1, s_2) = \int_{s_1}^{s_2} \left(\alpha(s') + \sigma(s')\right)\, ds'. \tag{3.9}$$

The zenith opacity refers to the opacity along the vertical path through the entire atmosphere - so when s_1 = surface and $s_2 = \infty$. Another way to look at the attenuation is through the transmission:

$$t(s_1, s_2) = e^{\tau(s_1, s_2)} \tag{3.10}$$

It indicates how much radiation of the original is present after propagation through the medium. A transmission of 1 indicates that the radiation is not attenuated and $t = 0$ indicates that the radiation is completely attenuated.

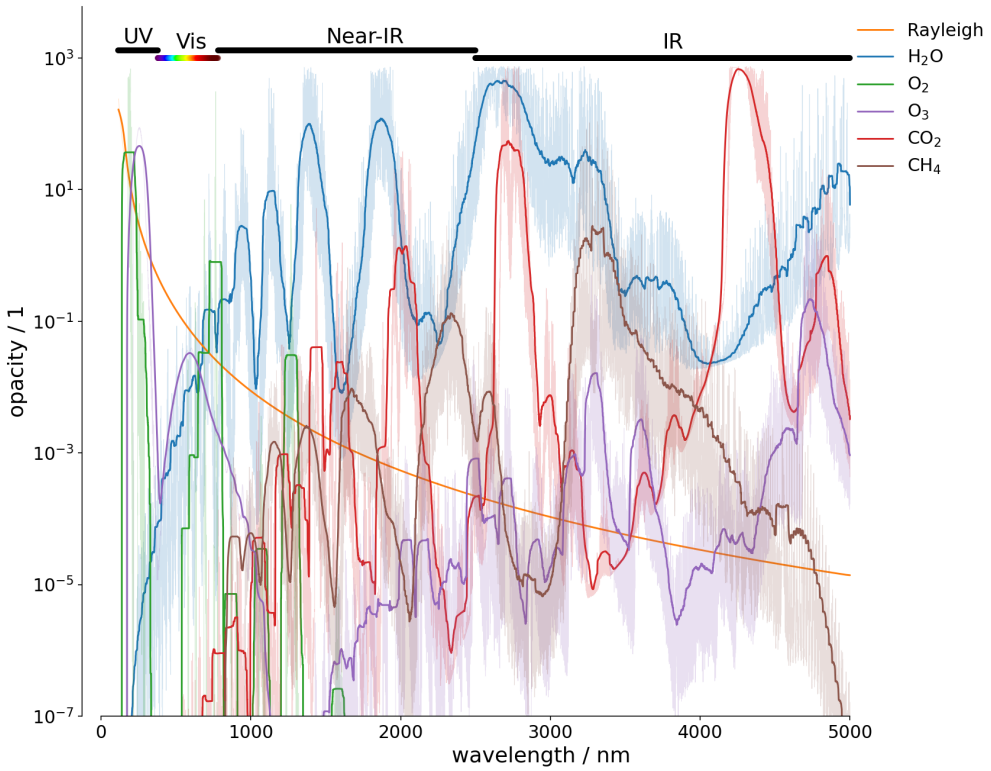

Figure 3.3: Spectrally resolved zenith opacity for the most dominant absorbers (water vapour in blue, oxygen in green, ozone in purple, carbon dioxide in red, and methane in brown) in the shortwave regime and the opacity due to gas scattering (orange) for a propagation path vertically through the atmosphere. The fine lines are calculated with a spectral resolution of about one-eighth of a nanometer. The heavy lines are a running mean of 500 frequencies.

The zenith opacities for absorption by ozone (O_3), water vapour (H_2O), oxygen (O_2), carbon dioxide (CO_2) and methane (CH_4), as well as the opacity due to gas scattering at the surface for a vertical propagation path (zenith angle = 0°), is shown in Figure 3.3. The strong wavelength dependence of the Rayleigh scattering is apparent, which scatters shorter wavelengths much more efficiently than larger wavelengths since it is directly proportional to the Rayleigh cross-section and this dependency is visible in Figure 3.2. In the UV region, the ozone band can be seen. This band ensures that the stratospheric ozone protects life on Earth from energetic UV radiation. In the VIS region, radiation is just weakly attenuated since the optical thickness drops to 0.1, and most of the radiation reaches the surface as it can be seen in Figure 3.4. Regions of low optical thickness are also called atmospheric windows. Most of the solar energy is present in this spectral range as it is shown in Figure 3.4. It is probably no coincidence that we call this band visible band since human vision probably evolved in this spectral region due to these very circumstances. Molecular oxygen has a strong absorption band in the UV region

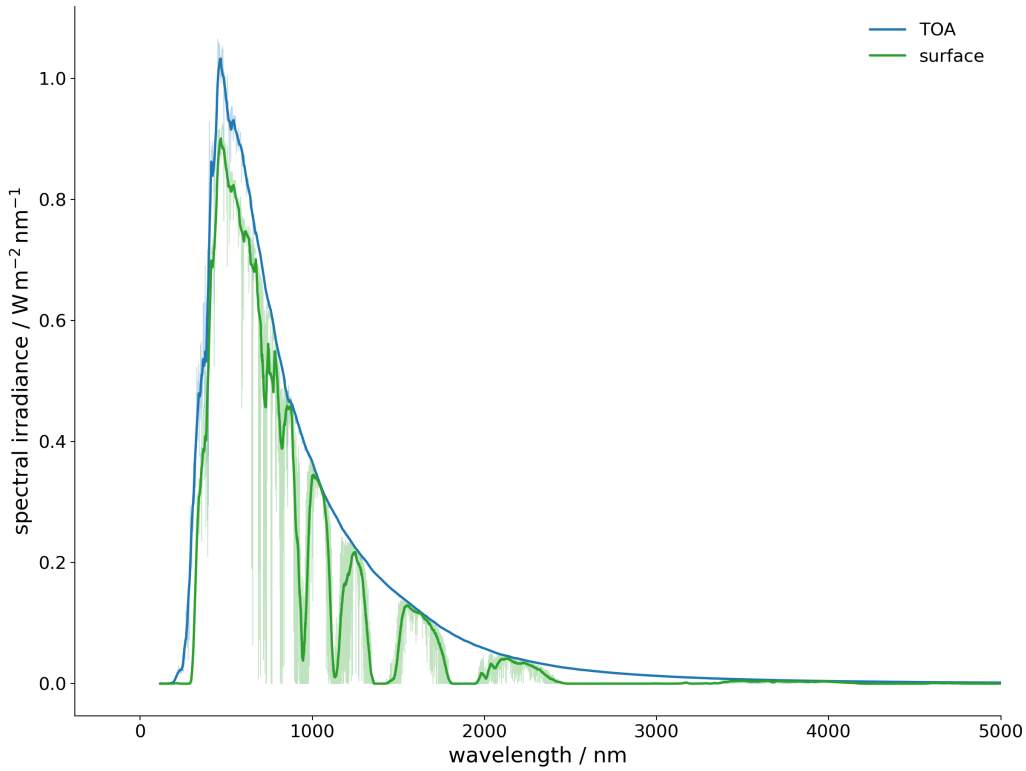

Figure 3.4: Spectral solar irradiance with a spectral resolution of about 0.3 nm (thin lines) at the top of the atmosphere (blue) and at the surface (green) for a solar zenith angle of 60° in a clear-sky atmosphere. The heavy lines are a running mean of about 30 nm.

at about 150 nm and is present at the longer wavelength edge of the visible at about 750 nm. The near-infrared is mainly dominated by water vapour with absorption bands at 700, 800, 900, 1100, 1400 and 1900 nm. Longer wavelengths are not discussed at this point since, in these spectral regimes, only a few percent of the total solar energy density is present and, therefore, it has hardly any effect on the spectral integrated shortwave irradiance. This can be seen in Figure 3.4 and will be discussed further in Section 3.4.

3.2.2 Planck radiation

The second term in the RTE (Eqn. 3.5) is the thermal source term, where I_B is the black-body radiation or Planck radiation with the respective emission temperature T. This term is dominant in the longwave regime as atmospheric temperatures are such that radiation in these bands is emitted. Thus it is called thermal emission. In which spectral regions thermal emission dominates is further discussed in Section 3.4 and more detail on Planck radiation itself can be found in Thomas and Stamnes [2002] as this thesis concentrates on the shortwave regime.

3.2.3 Scattering source term

As mentioned before, the scattering source term (term three in Eqn. 3.5) is a redistribution of radiative energy, as scattering transfers energy from the incidient direction to the scattered direction. Thus, the strength of the source is the same as the strength of the sink and is given by the approximation of the Rayleigh scattering coefficient from Equation 3.7 and the Intensity I_λ from the respective incidient direction. Radiation can be scattered from all directions and therefore an integration over the complete sphere (4π) is performed. Moreover, Rayleigh scattering has directional dependence. This dependence is described by the Rayleigh phase function P, which gives the angular distribution of the scattered light around the scatterer [Liou, 2002b].

$$P(\Theta) = \frac{1}{2}(1 + cos^2\Theta), \tag{3.11}$$

where Θ is the scattering angle, which is the angle between the incident and scattered beam described by the angles ϑ_{inc}, φ_{inc} and ϑ_{sca} and φ_{sca} [Mishchenko et al., 2002]:

$$\cos\Theta = \cos\vartheta_{inc}\ \cos\vartheta_{sca} + \sin\vartheta_{inc}\ \cos\vartheta_{sca}\ \cos(\varphi_{sca} - \varphi_{inc}). \tag{3.12}$$

Generally, the Rayleigh phase function is a phase matrix, because radiation can be described as a vector of length 4, which includes information on polarization. It is called the Stokes vector. The phase matrix is defined in the scattering plane. Thus one has to transform the Stokes vector with respect to the scattering plane. This transformation can be found in Mishchenko et al. [2002]. In the shortwave regime, radiation is generally partially polarized. For example, polarization is a basic part of a description of scattering of sunlight in a clear atmosphere. ARTS can simulate fully polarized radiation. However, for the purpose of this thesis, just the first element, the intensity, will be considered.

Of course, the scattering or reflection at the surface also contributes importantly. How exactly the surface reflects can be expressed with the help of the bidirectional reflectance distribution function ρ. For the sake of simplicity, it is only stated here that Lambert scattering is assumed for all parts of this work. Here, the irradiation hitting the surface is reflected uniformly in all spatial directions. In ARTS it is also possible to simulate specular reflections and Fresnel surfaces. However, the type of surface does not matter for the fluxes, which are the main focus of this work. This will be discussed in more detail in Appendix Section 8.3.

3.2.4 Solar radiation

To handle the solar source term, the concept of separating the radiation field into a direct and diffuse field is introduced. The direct field holds information about the radiation coming directly from the Sun. Hence it is also called direct beam. The total radiation field is the sum of the diffuse and the direct field. The solar flux $F_{\odot,r}$ is the attenuated

radiation from the top of the atmosphere (with position z_∞) along the propagation path to the position r:

$$F_{\odot,r} = F_{\odot,TOA}\, exp\left(\int_r^{z_\infty} k(s)\, ds\right), \tag{3.13}$$

where $F_{\odot,TOA}$ is the solar flux at the top of the atmosphere. How $F_{\odot,TOA}$ is implemented in ARTS is described in the Appendix Section 8.1. For the direct beam, the collimated beam approximation is used as angular variability of the direction of the radiation is neglected [Thomas and Stamnes, 2002]. This is also called parallel beam approximation.

The diffuse field holds information on the scattered radiation. In ARTS's `iyClearsky` solver the only way the diffuse field is modified is by scattering from the direct beam ($I_\lambda = F_{\odot,r}$). This is called single scattering approximation. The radiation can only undergo a single scattering event and is then considered as part of the diffuse field. which is excluded from the scattering source term. Even in the case of exact forward scattering ($\Theta = 0^\circ$) the photon is not scattered again because it is considered as part of the diffuse field and scattering only occurs from the direct beam. The same argument holds for the reflection at the surface. After the reflection at the surface, the radiation is considered as part of the diffuse field and thus is not scattered again. With these approximations, the scattering term of the RTE can also be written as

$$\frac{dI_{\text{diffuse}}}{ds} = \sigma\, P(\Theta_\odot) F_{\odot,r}, \tag{3.14}$$

where $\Theta_\odot$ is the scattering angle from the direction of interest to the direct beam.

To account for multiple scattering, the diffuse field is accounted for in the scattering source term. Depending on how man scattering orders one wants to account for, one has to update the diffuse field iteratively. DISORT uses such an approach.

More details on the radiative transfer equation and other effects one might want to consider can be found in Liou [2002a], Thomas and Stamnes [2002], Mishchenko et al. [2002], Chandrasekhar [2013].

3.3 Radiative Transfer Solver

In this section it is briefly explained how the `iyClearsky` works and how the solar source is included. The name `iyClearsky` indicates that it solves the RTE for the monochromatic pencil beam radiance `iy` and the measurement vector `y` at clear-sky conditions.

Figure 3.5 shows a schematic illustration of the `iyClearsky` solver. The atmosphere is illustrated as multiple lines because atmospheric properties are defined on these levels and those properties are changing linearly in $\ln(p)$, where p is pressure, between levels. ARTS is a 3D model (1D or 2D simplifications in the longwave are possible) for all simulations in the shortwave regime but in a commonly-used approximation is that the Earth is assumed to be flat. The surface is indicated with a brown line. It can have different

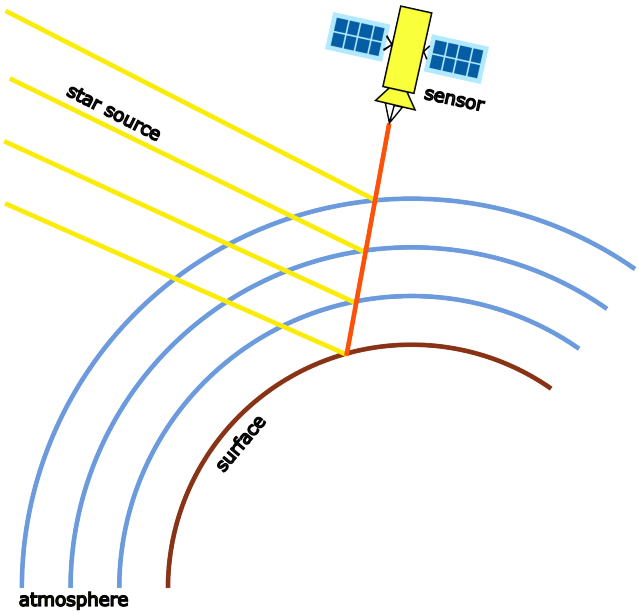

Figure 3.5: Schematic illustration of the iyClearsky solver.

properties as described in Section 3.2.3. The satellite represents a sensor at the location where the radiation is measured or for which the simulation is performed. The red line is the radiation's propagation path (ppath) towards the sensor. In the simplest case, an atmosphere without refraction is the geometric path of the sensor's line of sight. Intersections from the ppath with an atmospheric layer are here called ppath points. Along the ppath, the RTE is solved step-wise from the furthest to the nearest ppath point. Between every ppath point, the radiation is attenuated due to absorption and scattering (first term in the RTE) and radiation is emitted according to the Planck law with the respective temperature (second term). For the solar source term, a transmission (the beam is just attenuated along its path) simulation is performed along the ppath from the Sun to the respective ppath point of the measurement vector. This gives $F_{\odot,r}$ and is indicated by the yellow lines in the illustration. Note, that they are not divergent but parallel because they represent the collimated beam approximation. Then the scattering term (third term in Eqn. 3.5) is evaluated. This is the single scattering event described in Section 3.2.3. The scattering could also be the reflectance at the ground.

In contrast to the `iyClearsky` solver, DISORT uses a plane-parallel geometry and uses multiple scattering as described in Section 3.2.4.

How these concepts are actually implemented in simulations, so how the Sun is integrated into a simulations run script is shown in Appendix Section 8.2.

3.4 Distinction of spectral regimens

This section gives a more detailed understanding of why shortwave, solar radiation can conceptually be treated separately from longwave, thermal radiation as already mentioned in the introduction.

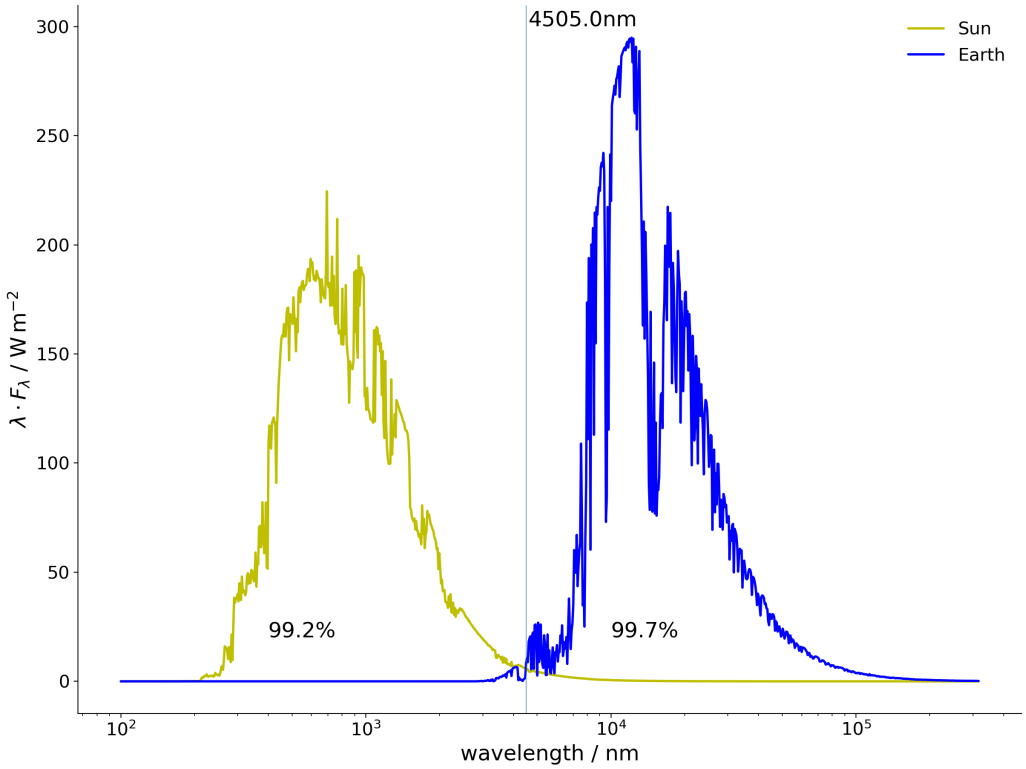

Figure 3.6: First mode of net shortwave (yellow) and outgoing longwave (blue) radiation at TOA. The net shortwave radiation is scaled by a factor of 4. The vertical line shows the crossing point of both spectra at 4541 nm (about 2202 kayser or 415 THz). Both spectra are simulated with ARTS.

Figure 3.6 shows the Earth's emitted outgoing longwave radiation (OLR) and the scaled net shortwave radiation emitted by the Sun. Both spectra are simulated with an atmosphere consisting of N_2, O_2, H_2O, CH_4, CO_2, N_2O and O_3, which are either an important absorption species in one or both regimes or are essential for the correct number density to represent a realistic Rayleigh scattering coefficient. For the shortwave simulation, the thermal emission is neglected and for the longwave simulation, no solar irradiation is present. The net spectral irradiance of the Sun is the difference between the incoming and outgoing shortwave radiation at TOA. Additionally, it is scaled by a factor of 4 to account for the spherical shape of the Earth and therefore represents a global mean shortwave net flux. The simulation itself is done in the tropics with the Sun in the zenith. The irradiance is also scaled with the wavelength to compensate for the varying size of the area elements due to the logarithmic scaling of the wavelength. Thus the energy equilibrium of the Earth becomes directly evident because the shortwave energy income is balanced with the outgoing longwave radiation. Therefore, the surface temperature of

the Earth stays roughly constant (the areas are not matching precisely because the simulation is performed for a profile representing the tropics (see Sec. 2.2.3) and not a global average. However, the Earth's energy budget is beyond the scope of this thesis and is not discussed further.).

The key message in the context of this thesis rather is, that there is little to no overlap between both regimes. The intersection of both curves is at about 4505 nm (about 2220 kayser or 4158 THz). 99.2 % of the net shortwave radiation is on the left side of the intersection, and 99.7 % of the longwave radiation is on the right side. This allows for the distinction and separate treatment of both regimes. The shortwave domain is dominated by solar radiation and thus the solar source term in the RTE (Eqn. 3.5) is essential and the Planck emission term can be neglected. Vice versa, in the longwave, the Planck emission term is dominant and the radiation is dependent on the thermal structure of the atmosphere [Petty, 2006]. Thus the longwave domain is often called thermal radiation due to the thermal emission that drives it. Here, the solar source term can be neglected, which was obviously the case in earlier ARTS versions, as the solar source term is introduced in the context of my work.

However, it must be said that this separation is a theoretical concept. ARTS can combine all spectral regimes in one simulation, which obviously corresponds to reality. In fact, one should simulate beyond the intersection in order not to lose up to a percentage of the total energy. However, the separation can be a useful concept for investigating different effects. ARTS previously exploited this as no solar source term was present until now. Yet the simulation where correct, since it was used to simulate effects in the IR and microwave range and the error of not having a solar source term is negligible as shown.

4 Simulations in the shortwave

This chapter is devoted to simulations in the shortwave regime. It will be explored what one needs to consider and what insights can be gained with the first ARTS simulations including a solar source term. For this purpose, first, the two radiative transfer solvers `iyClearsky` and DISORT are compared against each other. Therefore, the different geometry of both solvers is discussed and the radiance is analyzed in dependence on the zenith angle as well as the spectral dependency. Afterwards, the dependence of the spectral grid as well as the influence of the solar reference spectra on the shortwave flux is analyzed. These findings are then used for simulations, which are then analyzed for reasonableness and consistency. Important insights about simulating fluxes in the shortwave regime are gained and collected.

4.1 Simulation setup

This section describes the setup and settings used for the simulations contained in this chapter. The atmospheric profile of temperature, pressure and species concentrations are taken from the FASCOD tropical atmosphere (see Sec. 2.2.3). The chosen species are nitrogen (N_2), oxygen (O_2), water vapour (H_2O), carbon dioxide (CO_2), ozone (O_3), methane (CH_4) as they are either an important absorption species in the shortwave regime [Vardavas et al., 2011] or play an essential role for the correct number density to represent a realistic Rayleigh scattering coefficient. Profiles of the volume mixing ratios (VMRs) of these species as well as the temperature and pressure profiles of the atmosphere are shown in Figure 4.1. These will later be used to describe and explain features in radiances and irradiances.

All line and cross-section data are taken from the ARTS xml and cat data [artsxml, artscat]. For water vapour, the MT_CKD continuum version 3.5 self- and foreign continua [Mlawer et al., 2012] with a line cutoff of 750 GHz [Paynter and Ramaswamy, 2011] are considered as well as collision-induced absorption for N_2, O_2, and CO_2 [Richard et al., 2012]. Line mixing is turned off, as the continuum accounts for it. If fluxes or spectrally integrated values are discussed, they are integrated over the spectral grid described in Section 4.3. For the solar spectrum, the NOAA solar spectrum of May 2004 is justified in Section 4.4 with a total solar irradiance of $1360.088\,\mathrm{W\,m^{-2}}$ for the specific spectral grid. The simulations are using a Lambertian surface with a surface reflectivity of 0.3.

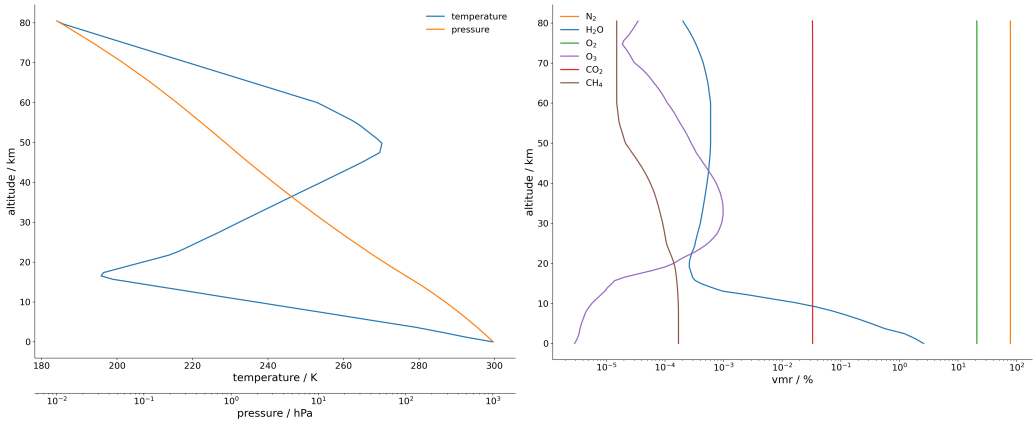

Figure 4.1: Profiles of temperature and pressure (left) and VMRs of used species for the simulations (right) of the tropical FASCOD reference atmosphere.

4.2 iyClearSky vs. DISORT

This section will study the differences between the ARTS internal solver `iyClearsky` and the integrated solver DISORT in more detail. In the following I discuss, the relative error from `iyClearsky` to DISORT, since DISORT is a well-established and tested solver and thus provides a good reference for our solver. Since `iyClearsky` is not (yet) optimised for irradiances, this section will analyse the radiation in radiances, the directed radiation unit. This is because integrating radiances spatially to irradiances in the optical is not as straightforward as in the longwave regime because of the spikiness of the solar beam. The goal is to eliminate the error due to different integration schemes.

First, the different geometries of the two solvers are discussed and how errors due to them can be minimized. Then the differences are analyzed in height resolution and for different zenith angles. Finally, the differences are investigated spectrally.

4.2.1 Geometry

One difference between `iyClearsky` and DISORT is the geometry, as spherical and plane-parallel geometry are used, respectively. In the plane-parallel assumption, Earth's curvature is neglected, and a flat surface with an atmosphere of parallel (often homogeneous) layers spanning infinitely in the horizontal dimensions is assumed. This geometry is often used when solving radiative transfer problems because of its computational efficiency and simplicity. The approximation works for rather large observational zenith angles up to 60 degrees [Dahlback and Stamnes, 1991].

The accuracy of this approximation can visually be confirmed with Figure 4.2. Here, the depth of the atmosphere from 1 % of the surface pressure to the surface is shown to scale with the horizontal scale. This shows how the Earth is almost flat compared to the vertical extent of the atmosphere. The red line represents a viewing angle of 60 degrees. This is also confirmed at [libradtran], where they stated that the irradiance of a direct source in the plane-parallel approximation is underestimated by 2 % at a solar zenith

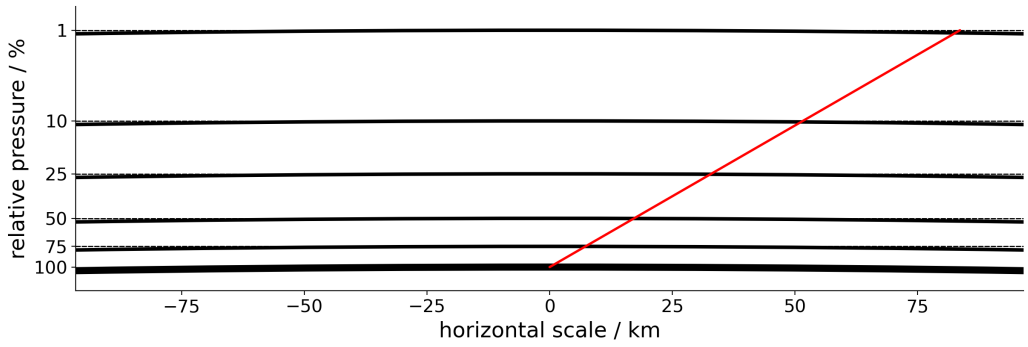

Figure 4.2: Illustration of the plane-parallel assumption as used in DISORT: The heavy line at the bottom represents the surface of Earth. The lighter lines above are lines of constant pressure of 1, 10, 25, 50, 75 % of the surface pressure. All these lines are arcs of circles, concentric with the Earth's centre. The dotted lines indicate the respective plane-parallel height. The top (1 % of surface pressure) is about 48 km above the surface. The red line represents a viewing angle of 60 degrees.

angle of 60 degrees and a wavelength of 310 nm. The approximation is even more accurate for larger wavelengths because less scattering occurs since the Rayleigh scattering coefficient strongly decreases with increasing wavelength. In the following section, to

minimize the error due to the different geometries, the Earth's radius for the simulations with `iyClearsky` is increased by a factor of 1000, and the distance of the Sun is adjusted accordingly to match the total solar irradiance.

4.2.2 Zenith angle

To compare the two solvers, the relative difference or error between the radiance simulated by `iyClearsky` to DISORT is used. In the left panel of Figure 4.3 the simulated radiances by DISORT for different altitudes and observational zenith angles are shown. The Sun is slightly offset of zenith (with 0.5 degrees) so that only the diffuse field is analyzed. The radiance field is mainly dominated by a vertical gradient. This gradient arises because the pressure decreases exponentially with altitude (see Fig. 4.1). As a result, the density increases strongly towards the surface and more scattering occurs since the Rayleigh scattering coefficient depends on the number density. There is also a comparatively weak dependence on the zenith angle. This is due to the fact that the path through the atmosphere becomes longer and more scattering occurs due to the longer distance. The relative error of the radiance simulated by `iyClearsky` compared to DISORT can be found in Figure 4.3. A negative error means `iyClearsky` underestimates the radiation compared to DISORT. Noteworthy are the red areas in the uppermost levels. These arise from the fact that below about 10^{-8} times the driving radiation DISORT cannot resolve enough significant digits [Stamnes et al., 2000] and this results in zero radiance, leading to an infinitely high relative error. Besides that, it is evident that `iyClearsky` generally

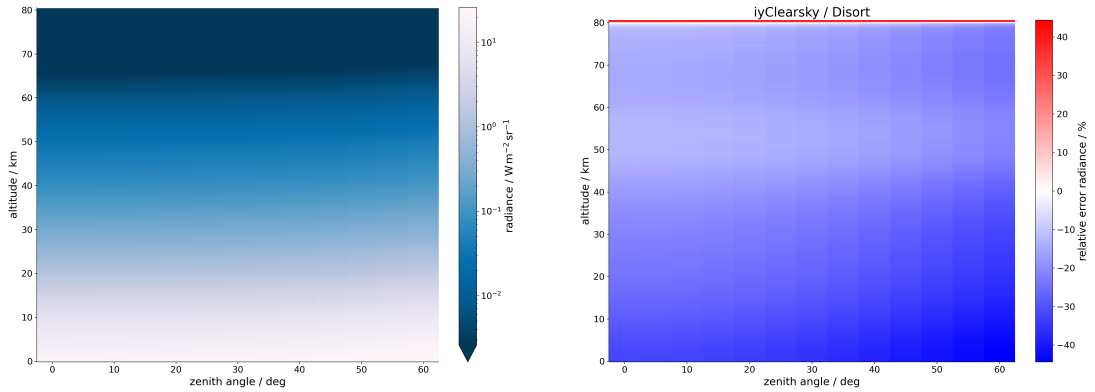

Figure 4.3: Radiances simulated by DISORT (right) and relative error of the radiance simulated by the iyClearsky solver to DISORT (right) for different altitudes and zenith angles.

underestimates the radiance of the diffuse field overall heights and zenith angles. This is also to be expected since DISORT is a multiple-scattering solver and thus higher-orders of scattering are considered in comparison to `iyClearsky`. In particular, the scattering from the direct beam, after it got reflected on the surface, is lost. Since in `iyClearsky` the reflection on the surface is considered a scattering event, the upward radiance from the reflection of the direct radiation cannot be scattered again in the downward direction. This explains the relative error of over 30 % near the surface since the albedo in the simulation is 30 % and thus this proportion of radiation considered in the scattering source term is missing. Hence, less radiance is scattered and the diffuse field is underestimated drastically by `iyClearsky`. This also leads to an underestimation of diffuse downward flux at the surface of at least 30 %.

A vertical gradient is also present in the relative error since in lower altitudes more radiation is scattered. The higher-order scattering terms have a stronger effect. At the surface and a zenith angle of 0 degrees, the relative error is 32.3 %. The additional 2.3 % in relative error is caused by the difference between single and multiple scattering. The relative error also increases with the zenith angle. Here, higher-order scattering terms become more important because the effective path through the atmosphere becomes longer and more radiation occurs. This results in an additional relative error at the surface of 14.4 % with a zenith angle of 60 degrees. Since downward irradiances are integrated over all downward irradiances and higher zenith angles are less important, the error in the diffuse downward flux is estimated to be in the order of 5 %. The error in the flux of the direct beam will be equal to the relative error of the radiance. Here, the observation zenith angle should be understood as the solar zenith angle.

However, with those arguments, the relative error should monotonously increase towards the surface and with zenith angle, but between an altitude of around 60 km to 50 km the error decreases towards the surface. This effect is even more dominant at higher zenith angles. This can not be affected by the difference in scattering order between the solvers. I assume it is caused by the plane-parallel geometry of DISORT be-

cause an increase in the Earth's radius reduced the strength of this effect. Dahlback and Stamnes [1991] also describe an error in these heights caused by the different geometries. This is described only for larger zenith angles, and the error decreases with smaller zenith angles. However, since small absolute values are compared, it can lead to noticeable relative errors.

4.2.3 Spectral dimension

This section investigates the differences between `iyClearsky` and DISORT spectrally resolved. To address this, the relative error of the spectral radiance simulated by the `iyClearsky` solver compared to DISORT at different altitudes and a solar zenith angle of 60 degrees is shown the upper panels of Figure 4.4. In the upper left panel of Figure

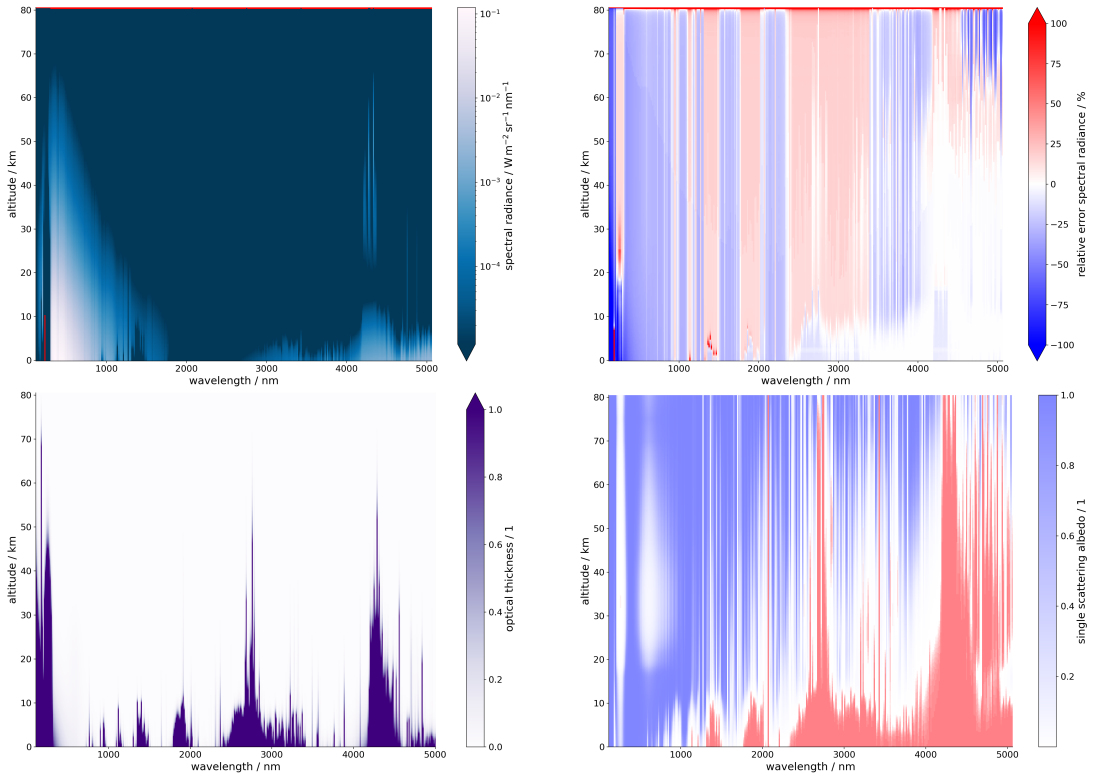

Figure 4.4: Radiance simulated by DISORT (upper left), the relative error of the radiance simulated by the iyClearsky solver to DISORT (upper right), integrated optical thickness (lower left), and single scattering albedo (lower right) for different altitudes and frequencies for a zenith angle of 60 degrees.

4.4 the radiance simulated by DISORT is shown for altitudes ranging from the surface up to 80 km and from 115.5 nm to 5000 nm. Most striking are the high spectral radiances at wavelengths from 300 nm to 1800 nm as the diffuse field is dominated by Rayleigh scattering. This can be seen clearly as the transition from whitish to dark blue colour, i.e. the same spectral radiance, decreases in altitude towards higher wavelengths. This is because at higher wavelengths, higher number densities are needed to compensate for the decreasing Rayleigh scattering coefficient. The highest spectral radiances are at around

360 nm because on the one hand, this region has the least absorption (see Fig. 3.3), and on the other hand, the product of Rayleigh scattering coefficient and the radiance from the solar reference spectrum (see Fig. 3.4) is greatest around that region. The spectral radiance increases towards the surface, as previously observed since this spectral region has the highest intensity and thus determines the structure for the spectrally integrated radiances. In the troposphere, at 900 nm, 1100 nm and 1300 nm the spectral radiance decreases towards the surface, as radiation is absorbed by water vapor (see Fig. 3.3). These water vapor bands can also be seen in the vertical integrated optical thickness in the lower left panel of Figure 4.4.

Although the Rayleigh coefficient is strongest in the UV region, the sun emits less radiation and the radiation that is emitted is almost fully absorbed by the ozone (see Fig. 3.3 and lower left panel of Fig. 4.4).

In the near-IR region, the thermal emission can be seen. It is strongest near the surface, as temperatures, as well as density (absorption coefficient is exactly dependent on the number density), are high. Around 4300 nm in the stratosphere strong emission of CO_2 is present. There, temperatures and number density are high enough to emit noticeable radiation.

Noteworthy is that at 230 nm the ozone and oxygen absorption is so high (see Fig. 3.3), that DISORT numerically cannot resolve it for the above-mentioned reasons.

In the upper right panel of Figure 4.4 the relative error between `iyClearsky` and DISORT is shown. Blue colours and thus a negative relative error mean an underestimation of the radiance by the `iyClearsky` solver compared to DISORT. Unlike the spectrally integrated radiances described above, in some spectral bands `iyClearsky` overestimates the spectral radiance compared to DISORT and this is shown in red. In general, the relative error shows a high degree of spectral structure. At the uppermost level, the relative error is again infinity. However, the relative error propagates downwards, because, if the spectral radiance is underestimated at one point, this will be the case for all point down the propagation path, if the physics are the same. I suspect that this is the case for the reddish bands in the near-IR. Generally, good insight into the overall structure is provided by the single scattering albedo, which is the ratio of the scattering coefficient to the extinction coefficient (sum of absorption coefficient and scattering coefficient) [Stamnes et al., 2000, Vardavas et al., 2011]. It ranges between 0, where only absorption is occurring and 1, where only scattering is of importance. Thus, it can be interpreted as the probability of a photon undergoing a scattering event instead of an absorption event. The single scattering albedo is shown in the lower right panel of Figure 4.4. In regions, where scattering is important, the numerically induced error at the uppermost levels is quickly compensated and `iyClearsky` underestimates the radiation. In regions where absorption dominates or neither is important this error propagates downward. However, this has close to no influence, since in regions such as the near-IR, there is little spectral

radiance and thus the absolute error is negligible.

In the shortwave, which dominates the structure of the spectrally integrated radiance, which was described above, the spectral radiance is overall underestimated by `iyClearsky`. The vertical gradient is also present but is suppressed by the large scale of the colour bar because the scale of the color bar does not match the scale of the color of the right panel in Figure 4.3. Numerically this gradient matches.

In the UV region at about 250 nm in the stratosphere `iyClearsky` overestimates compared to DISORT. At these altitudes, stratospheric ozone is a dominant absorber (see Fig. 4.1). This absorption-dominated region extends from 20 km up to about 60 km with a maximum at around 30 km. The maximum in the relative error is at 25 km with 95 % overestimation by `iyClearsky`. I suspected that this is due to the multiple scattering. The effective path length gets statistically longer for each photon as it gets scattered back and forth. Thus, in regions with high absorptivity, the radiation field gets more strongly attenuated, and the `iyClearsky` will overestimate it. Below these altitudes `iyClearsky` drastically underestimates compared to DISORT, because is lacks the scattering source of the reflected direct beam. The relative difference is so large because the diffuse field is relatively weaker due to the strong absorption above so even a small source leads to big differences. This effect can also be seen at the water vapor bands at 700, 800, 900, 1100, 1400 and 1900 nm, where the optical thickness strongly increases due to the moist troposphere (see lower left panel of Fig. 4.4 and Fig. 4.1).

In regions of thermal emission DISORT and `iyClearsky` agree well. There, all radiation is driven by the thermal emission and small differences due to scattering are overshadowed.

In the visible regime is an abrupt transition of the relative error in high altitudes, which decreases with height towards longer wavelength. It is assumed to be an artefact of Rayleigh scattering since it follows an isoline of the product of number density and scattering coefficient. It might be due to the numerical resolution of DISORT.

Since the radiances, and thus the irradiances, differ significantly, especially near the ground, the DISORT solver is used for all further simulations. A big improvement for `iyClearsky` would be to also consider the reflected directed beam for scattering.

4.3 Spectral grid

Radiative fluxes, also called irradiance, are spectrally integrated quantities (see Eqn. 3.2). Since these are unsmooth variables due to the many spiky and seemingly randomly distributed absorption lines, the choice of supporting points for the integration, i.e. the spectral grid, is of great importance. The risk is that by chance absorption lines are overrepresented in the choice of frequencies and thus more radiation is absorbed in the atmosphere. The flux would be underestimated and vice versa.

Buehler et al. [2006] have shown that a quasi-random and thus, also an equidistant grid in frequency space with a sufficient amount of frequencies, is a valid choice in the IR and larger wavelength since the number of absorption lines is approximately representative. I assume this holds for the shortwave regime and thus only equidistant grids in wavelength space are analyzed, in the following. Note that it is equidistant in wavelength and not in frequency. This is justified by the fact that not the lines themselves matter, but if the supporting points are evenly distributed a representative number of absorption lines are present.

To investigate the effect of the number of supporting points on the flux, simulations with spectral grids ranging from 115.5 nm to 9,999.5 nm and different numbers of frequencies are made. For the lower limit of the spectral grid, the smallest wavelength of the solar reference spectrum is taken. It is at 115.5 nm and thus just in the ultraviolet part of the spectrum. It is only a few hundred nm away from the maximum of the spectrum at 451.5 nm, and therefore it is not expensive to calculate the full range down to the lower part of the spectrum. However, the reference spectra are given up to 99,999.5 nm. For computational efficiency, I cut the equidistant wavelength grid at 9,999.5 nm. With that cut 0.06% of the total solar power density is missed. The error made is determined to be $0.82\,\mathrm{W\,m^{-2}}$. To compensate for the loss, the reference solar spectrum could be scaled in the way, that the needed total solar irradiance is present in the used spectral grid. This would mean an effective energy shift towards the shorter wavelengths. Another approach would be to use an equally spaced frequency grid for the frequencies above the cutoff. The spectral grid of choice extends from the short-wave regime, which normally goes up to 4,000 nm or 5,000 nm, into the near-IR/IR.

To determine the number of sample points, the stability of the flux for differently sized spectral grids is investigated. In order to evaluate only the influence of solar radiation, the thermal emission (the second term in the radiative transfer equation) is neglected. As a reference, a simulation with 131,072 (=2^{17}) frequencies is used. For the simulations with fewer frequencies, the reference spectral grid is split in half, resulting in two alternating spectral grids. This process is repeated 11 times which results in increasing numbers of simulations with smaller spectral grids. The number of simulations per spectral grid size can be found in table 4.1.

Downward fluxes at the top of the atmosphere (TOA) and at the surface are shown in the upper panel of Figure 4.5. As expected, the irradiances converge to a fixed value the more frequencies are used in the simulation. This is due to the fact that the numerical integration itself becomes more accurate simply because of the larger number of support points and that the hit rate of the absorption lines converges and gets closer to a realistic value. The simulated irradiances at the TOA converge faster than the irradiances at the surface because the radiation has not experienced any absorption in the atmosphere and only the smoothness of the solar spectrum has an influence on the resulting irradiance. The used solar spectrum has a finite resolution of one nanometer and therefore,

Number of frequencies	Number of simulations
131072	1
65536	2
32768	4
16384	8
8192	16
4096	32
2048	64
1024	128
512	256
256	512
128	1024
64	2048

Table 4.1: Number of simulations per spectral grid size.

from 10,000 simulated frequencies, which corresponds to a resolution of one nanometer, no further accuracy will be gained. The irradiances differ marginally because ARTS internally interpolates the solar spectrum exactly to the simulated frequency which causes variations and inaccuracies. In contrast, the absorption lines are calculated exactly for the respective frequency and, thus, theoretically, have an infinitely accurate resolution. Therefore, they do not become smoother with higher resolutions, but remain unsmooth, which leads to slower convergence. The standard deviation, which represents the variation within simulations with the same spectral grid size, behaves the same way. The absolute variation is always smaller at TOA than at the surface and decreases faster with an increasing number of frequencies.

The error of the mean irradiance of all simulations of one spectral grid size relative to the reference simulation with 131,072 frequencies is shown in the lower panel of Figure 4.5. This quantifies what is already described qualitatively in the upper panel. The error at the TOA is always smaller compared to the surface because the irradiances at the surface include the complicated and strongly frequency-dependent absorption that occurs when the radiation propagates through the atmosphere. Since this physics is already taken into account, it is redundant to consider upward fluxes in this investigation, since these would contain the same information, just with a larger amplitude. Since the aim of this study is to investigate the effect of the atmosphere on radiation, the irradiances on the surface are considered for the choice of the spectral grid. There the error compared to the reference simulation falls below $1\,\mathrm{W\,m^{-2}}$ (see black line in the lower panel of Figure 4.5) for the simulation with 32,768 frequencies, which corresponds to a spectral resolution of almost 0.3 nm.

Qualitatively, this number can be confirmed by Vardavas et al. [2011], who state that 200 frequencies are sufficient for the UV-visible spectral range from 121.6 nm to 850 nm, except for the highly structured Schumann-Runge band of O_2 from 180 nm to 200 nm, which requires a more precise resolution. This would mean that just under 2,500 fre-

quencies would be needed to cover the chosen grid with the entire short-wave regime and the near-infrared. This can be interpreted as a lower limit of sample points.

However, the frequency-dependent Doppler broadening cannot be neglected in the UV-visible range [Burrows et al., 2011]. The half-width of the line at the half-maximum α_D is

$$\alpha_D = \nu_0 \sqrt{2 \ln(2) \frac{KT}{mc^2}}, \tag{4.1}$$

where K is the Boltzmann constant, and T the absolute temperature, m the mass of the molecule under consideration, c the speed of light and ν_0 the frequency of the line maximum [Liou, 2002a]. Thus, the half-width at half-maximum of the absorption lines is linear with the frequency, which means that with a halving of the frequency twice as many frequencies would need to be simulated to achieve the same coverage of absorption lines. This means that more lines are required in the near-infrared. Start at $\nu_0 = 115.5\,\text{nm}$ and add points according to the half-width of the line at the half-maximum at that wavelength. One would need to simulate over 1 million wavelengths, with the most samples lying in the IR. However, a high line density at the IR side of the spectral grid where only a small fraction of the power density is present is inefficient. This can be considered as an upper limit, which, however, is not feasible in reality. One could follow the approach described earlier and use an equally spaced frequency grid for the IR which was proven to be sufficient [Buehler et al., 2006] and use an equally spaced wavelength grid in the shortwave.

For simulations in the shortwave, a spectral grid with 32,768 frequencies is a good compromise, because an equidistant grid is used, which is sensible for the reasons mentioned above. The visible regime, where half of the energy density is located, is covered more than necessary, but this is computationally feasible. The near-IR region, where almost the other half of the energy density is located, is sufficiently covered and the wing in the IR is not sufficiently covered but contributes only about 1% to the total irradiance. This can be compensated for with an energy shift within the chosen spectral grid. For all further flux simulations in this study, a spectral grid with limits from 115.5 nm to 9,999.5 nm and 32,768 equidistant wavelengths is used.

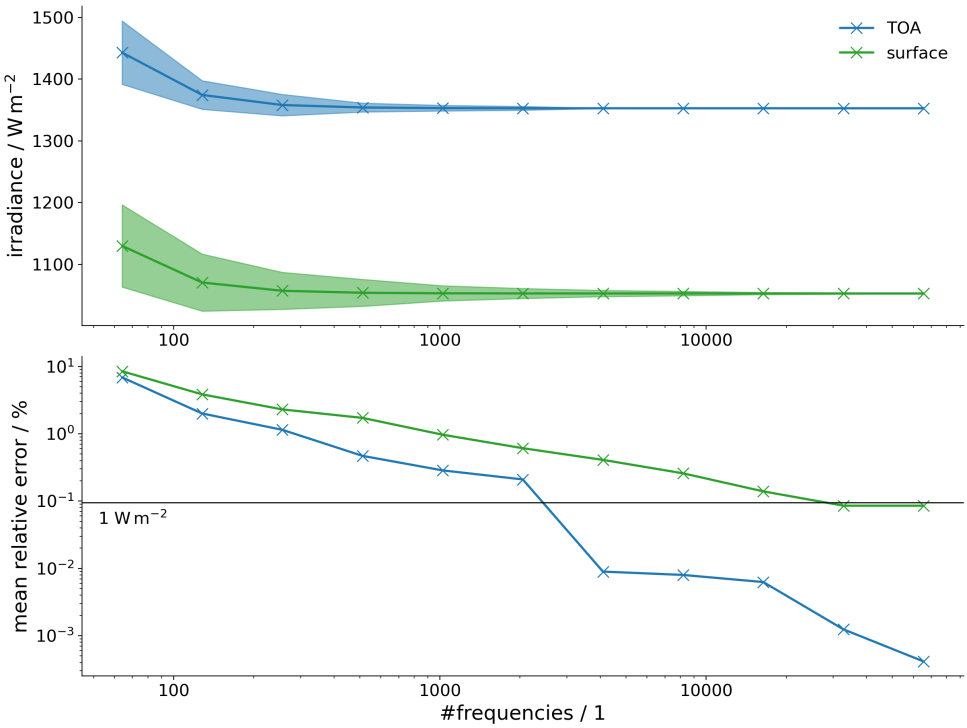

Figure 4.5: Downward irradiances at TOA in blue and at the surface in green simulated using spectral grids of different sizes. The respective shaded areas show the standard deviation of simulations with the same number of frequencies but a relative spectral offset to each other (upper panel). The mean error for TOA in blue and surface in green relative to a respective simulation with 131,072 frequencies and an error of 1 W m^{-2} relative to the surface reference simulation shown as the black line (lower panel).

4.4 Solar Spectrum

The choice of the solar reference spectra is vital as the Sun is the driving force for all radiation in the shortwave. Multiple solar reference spectra are provided in the Solar Irradiance Climate Data Record (see Sec. 2.2.1) because the solar activity changes over time. It undergoes an 11-year cycle with a variant number of sunspots from the order of 10 per year, called the solar minimum, up to hundreds a year, called the solar maximum. There is a period between 1645 and 1715 where the cycle is unclear due to very few sunspots, and this period is referred to as the Maunder minimum [Vardavas et al., 2011, NOAA]. Solar reference spectra for quiet, low, moderate and high solar activity and in the Maunder minimum are provided.

Sunspots produce slight variation in solar flux, but the magnetic field activity has a significant effect on the ultraviolet flux as at the Lyman-α line, the spectral irradiance in the UV can vary by a factor of 2 [Vardavas et al., 2011]. This can lead to differences in the total flux. Especially when compared to a blackbody Sun with the corresponding emission temperature. For further simulations, the spectrum with moderate solar activity from May 2004 is used as it is closest to an average solar activity.

4.5 Fluxes in the short-wave

Now all the settings have been clarified and are being applied for the first simulations. First, general down- and upward fluxes are shown. These fluxes are then analyzed spectrally and lastly, it will be examined how fluxes behave for increasing solar zenith angles. These simulations are analyzed for reasonableness and consistency. The aim is to gain general insights into simulating fluxes in the shortwave regime.

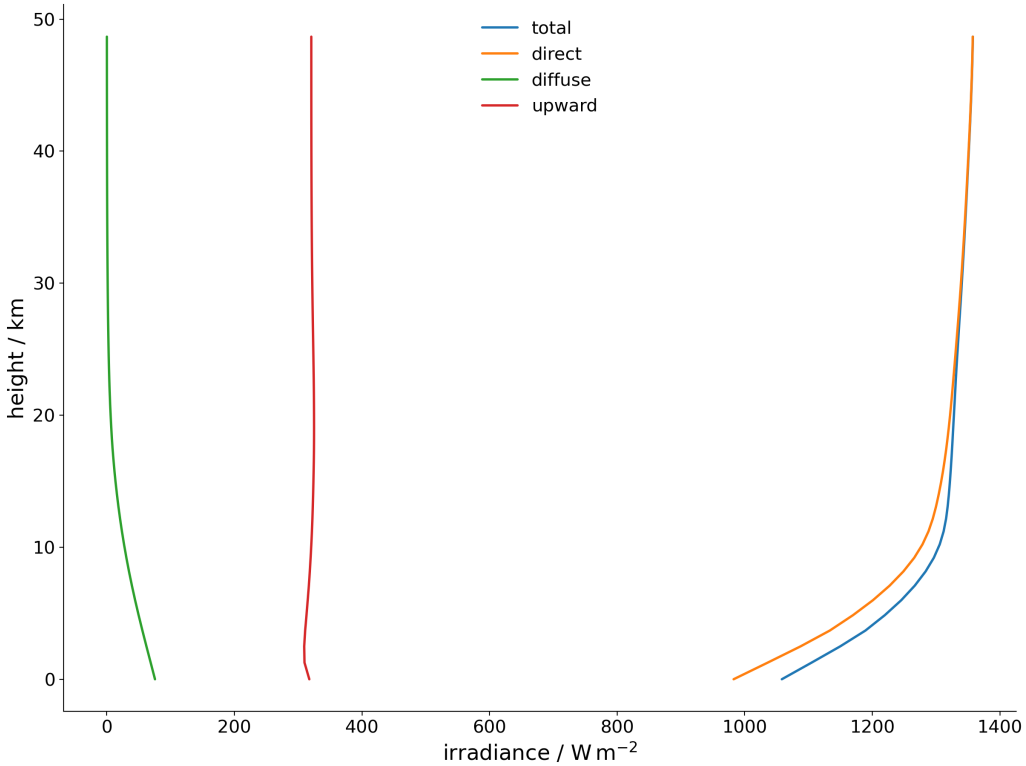

Figure 4.6: Profiles of the total (blue), direct (orange), and diffuse downward (green) irradiance, as well as the diffuse upward (red) irradiance for a solar zenith angle of 0 degrees.

Figure 4.6 shows profiles of the total, direct, and diffuse downward irradiance, as well as the diffuse upward irradiance. The irradiation is analyzed along the propagation path. Starting at the top of the atmosphere, the total downward flux has a value of 1360.088 W m^{-2} , which is the total solar irradiance. It is also called the solar constant and is the energy input of the earth. This value is the same as the given solar spectrum of May 2004 interpolated on the spectral grid for the simulation and spectrally integrated. The total downward irradiance decreases along its path towards the surface due to the attenuation of absorption and scattering of the direct beam in the upward direction. This gets exponentially stronger towards the surface because it is proportional to the number density.

The total downward flux is the sum of the direct downward and diffuse downward flux. At TOA the total downward flux consists just of the direct beam, as no scattering has

happened. Towards the surface, the total irradiance is attenuated due to absorption but the diffuse downward irradiance increases due to increasing scattering. The irradiance of the diffuse field is 75.5 W m^{-2} which is about 7.7 % of the direct beam at the surface. The diffuse downward field is increasing over all altitudes because more radiation is scattered than is absorbed. The downward diffuse field is not just fed by the forward scattering [1] of the direct beam but also by scattering from the upward radiation. Radiation is also scattered from the diffuse downward field into the diffuse upward field, but since the diffuse upward field is larger than in the diffuse downward field, there is a net gain in the diffuse downward field.

The upward irradiance at the surface is 30 % of the total downward irradiance as the surface reflectivity is 0.3. In the diffuse upward field scattering source and absorption sink are close to balance. It gets attenuated with height until an altitude of about 2 km. At this altitude, absorption and scattering in the upward direction cancel out. Above that, the scattering input dominates, and the upward irradiance is slightly increasing with height. Above an altitude of 25 km absorption again dominates slightly, and irradiance decreases with altitude. Absorption in this height is associated with the ozone layer (see Fig. 4.1. However, this is hardly noticeable because the atmosphere is so thin, so absorption and scattering are both weak.

4.5.1 Spectrally resolved fluxes

Figure 4.7 shows profiles of downward and upward spectral irradiance of different wavelengths in and around the visible spectral range. The distribution of downward spectral irradiance follows the solar spectra. Its peak (out of the plotted wavelengths) is at 480 nm and gets less to smaller and larger wavelengths. Absorption can be seen around 600 nm at an altitude of about 25 km. This is due to stratospheric ozone. At 720 nm, there is a strong water vapour absorption line (compare Fig. 3.3), and therefore the spectral flux is attenuated in the lowest four km, where most of the atmospheric water vapour is located. At 760 nm, there is a strong absorption line of O_2, and thus the spectral flux starts to decrease at about 15 km, where the atmospheric density starts to increase noticeably (O_2 concentration is constant with height). Another visible effect is the weakening of the downward flux due to Rayleigh scattering and its wavelength dependence. The shorter the wavelength, the more the downward flux is attenuated towards the surface. This can be distinguished from attenuation caused by absorption by looking at the upward fluxes. The shorter wavelengths near the surface increase with altitude because they experience a lot of scattering and thus, a lot of radiation is scattered from the diffusive downward field into the diffuse upward field. In contrast, as earlier mentioned, long wavelength fluxes decrease with altitude as they continue to be absorbed along their path. The ab-

[1] Note that forward scattering from the direct beam is technically only correct if the Sun is zenith. Because forwards describes a scattering angle smaller than 90 degrees. Thus, at low solar zenith angles forward scattering from the direct beam can also scatter into the diffuse upward flux.

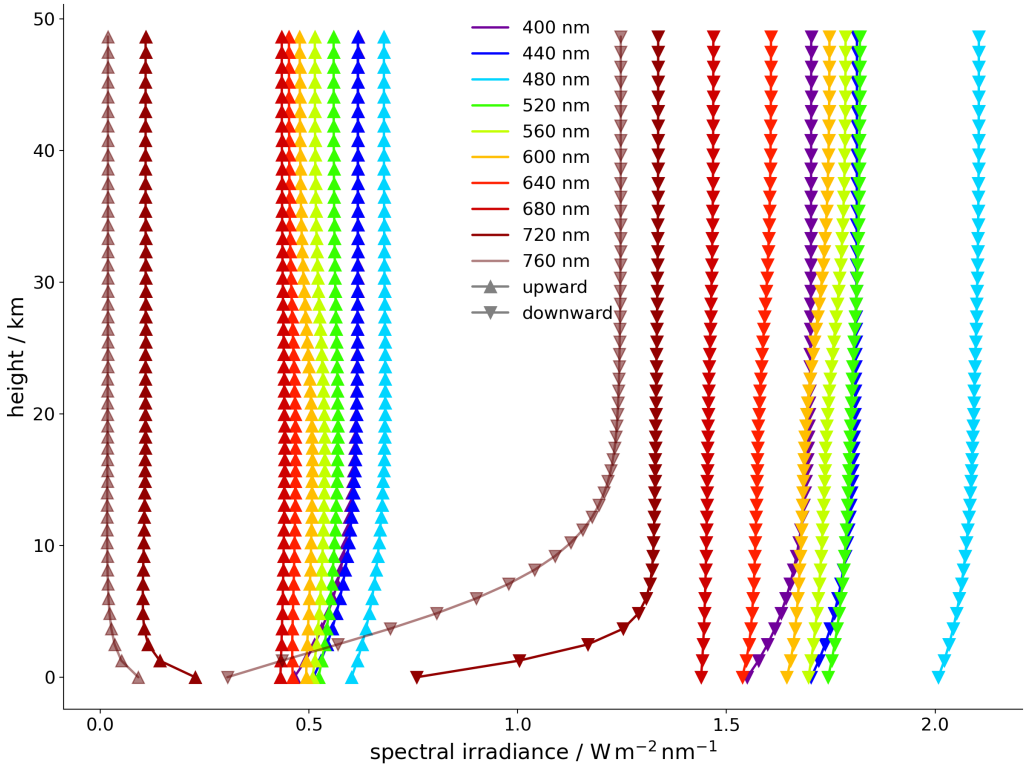

Figure 4.7: Profiles of downward (down point triangle) and upward (up pointing triangle) spectral irradiance of 10 different wavelengths in the visible spectral range. The colour of the line represents the human-preserved colour of the respective wavelength.

sorption due to stratospheric ozone can also be seen in the upward fluxes as the spectral irradiance slightly decreases with height. Fluxes at wavelengths not strongly affected by absorption or scattering stay about constant in height. Again, the surface reflectivity is 0.3, and therefore, the upward fluxes at the surface are 30 % of the downward fluxes at the surface.

4.5.2 Solar zenith angle

In this section, the dependence of the irradiance on the solar zenith angles is investigated. Figure 4.8 shows the downward irradiance at TOA and the surface for different solar zenith angles, as well as the associated theoretical lines if the decrease were cosine-shaped. For a solar zenith angle of 0 degrees, when is Sun is directly above the sensor, the values match the values of TOA and at the surface of the total downward irradiance in Figure 4.6, respectively. At TOA the simulated irradiance decreases cosinusoidally with solar zenith angle since the radiation has not yet undergone any change due to propagation through the atmosphere. Thus, the decrease is determined by the projection onto the surface element dA and this projection decreases cosinusoidally with the incidence angle, which is, in this case, the solar zenith angle. Therefore, both curves match per definition. The irradiance at the surface is always lower than at TOA due to the attenuation caused

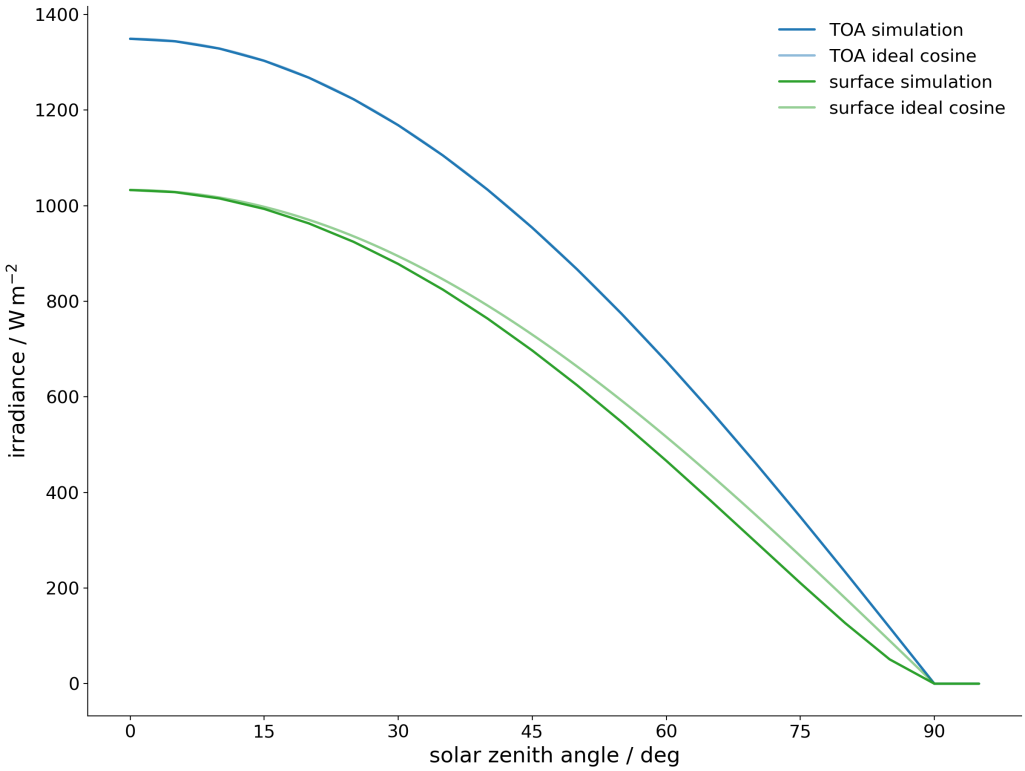

Figure 4.8: Downward irradiance for different solar zenith angles and plane-parallel geometry. One simulation is performed at TOA (blue) and the other at the surface (green). The transparent lines describe a cosine decrease with the solar zenith angle. At TOA these lines align.

by absorption in the atmosphere (see also Fig. 3.4). The shape of the irradiance curve of the surface is similar as the projection on the surface element decreases as well. However, the simulated irradiance is always less than or equal to the irradiance if it were cosinusoidally decreasing. In fact, the difference becomes larger with increasing solar zenith angle until they both reach zero at a solar zenith angle of 90 degrees. This discrepancy is due to the greater effective path length that the radiation must pass through. The optical depth is monotonically increasing with the path length (see Eqn. 3.9) and thus more radiation attenuated. For higher solar zenith angles than 90 degrees, the irradiance is zero. Realistically, some irradiance could be measured at solar zenith angles slightly above 90 degrees, because although no direct solar radiation reaches the surface, solar radiation will be scattered high in the atmosphere towards the surface. However, the calculation is performed with the plane-parallel solver DISORT, which cannot simulate solar zenith angles above 90 degrees because the surface is horizontally infinitely extended. Thus the Sun cannot disappear behind the horizon.

As it was previously described, the plane-parallel approximation becomes inaccurate towards zenith angels above 60 degrees (see Sec. 4.2.1). This applies to the angle of observation as well as to the angle of incidence of solar radiation.

5 RFMIP

This chapter uses the RFMIP (see Sec. 2.2.4) atmospheres for simulations in the shortwave regime. In the context of Pincus et al. [2020], these atmospheres are used to evaluate radiative transfer models in their estimation of radiative forcings. The radiative forcing is the change between present-day and preindustrial conditions in net downward flux at the top of the atmosphere (TOA) and the surface, and the change in net absorption across the atmosphere (net flux at TOA minus net at the surface). However, the objective of this chapter is to evaluate possible weaknesses and limitations in ARTS simulations of the shortwave regime in order to identify which further improvements could be made. Thus, not the radiative forcings are compared, but simulated irradiance for the 'present-day' scenario. ARTS simulations are compared to the line-by-line model LBLRTM [Clough et al., 2005] and RRTMG, which utilizes the correlated-k approach for application to global climate models [Mlawer et al., 1997]. One would expect results to be closer to the LBLRTM model because ARTS and LBLRTM are line-by-line models which are physically more 'pure' and derived from first principles compared to RRTMG, which is a parameterisation optimized for efficiency and speed as its application is in General Circulation Models. In the first section, the simulation setup and data preparation are described (see Sec. 5.1) and in the subsequent section, results of the RFMIP simulations are shown and compared (Sec. 5.2).

5.1 Setup and data preparation

In the context of the RFMIP (see Sec. 2.2.4), atmospheric conditions for 100 different sites are given for 18 different experiments. The experiments represent conditions in different epochs or climate scenarios. For this work, only the 'present-day' experiment was used. For all sites, the position (latitude, longitude), surface temperature, emissivity, and albedo, as well as the total solar irradiance and solar zenith angle, are given. Temperature and pressure are given on 61 vertical levels. For these levels, the fluxes are simulated. The atmospheric composition is defined for the layers between these levels, where only water vapor and ozone change with height. All other species are constant with height and also at all sites. The concentration of all species is given in mole fraction but ARTS used volume mixing ratios as input. However, these units are numerically identical. A list of all species can be found in the Appendix Section 8.4. Some species were not part of the ARTS-cat-data and therefore are not considered in the simulations. It is assumed that the effect of these species on the flux is negligible, as they are minor trace gases

with low concentrations and have no significant bands in the shortwave regime. As in the previously shown simulations, the MT_CKD self- and foreign continua (version 3.5) [Mlawer et al., 2012] with a line cutoff of 750 GHz [Paynter and Ramaswamy, 2011], as well as collision-induced absorption for N_2, O_2, and CO_2 [Richard et al., 2012], are used. Line mixing is turned off as the continua account for it. As the aim is to evaluate the shortwave fluxes, no Planck emission is present. Since no spectral grid is given, the grid defined in Section 4.3 is used. For the angular resolution, 10 streams (discrete ordinates in DISORT) are used.

ARTS internally also needs information about the altitude. This is calculated using the barometric formula, assuming hydrostatic equilibrium. This determines the height with respect to a reference height. For the reference point, the surface elevation of the respective location was determined with the help of the open elevation public API [open API].

The strength of the solar source is specified by the total solar irradiance (TSI). The TSI varies between sites to account for the different distances $d_{\odot,p}$ between the Sun and the Earth due to Earth's elliptical orbit. The distance is 0.9832899 au in the perihelion and 1.0167103 au in the aphelion, which are the closest and farthest points, respectively. The difference in distance can make up a difference of 6.93 % in flux at the TOA. It is crucial to simulate the correct total solar irradiance because it is the driving mechanism for all radiation in the shortwave. Minor errors at the top of the atmosphere propagate and grow as the radiation propagates through the atmosphere. Thus, the Sun reference spectra are scaled by the ratio of the solar constant of the reference spectra and the target TSI. The solar constant of the reference spectra is calculated for the specific spectral grid used for the simulation. The reference spectra are defined in the way that they match the TSI at TOA at the subsolar point (see Sec. 8.1). However, ARTS is a 3D model and the radiation at TOA is simulated from the Sun's centre towards the Earth (according to the inverse-square-law). This distance between TOA and the Sun is greater in simulations where the Sun is not in the zenith. Thus, the irradiance there is smaller than at the subsolar point. This can be seen in the illustration in Figure 5.1. There, the distance from the simulation point (sim) to the Sun (R_{sim}) is greater than the distance from TOA at the subsolar point (ssp) to the Sun ($R_\odot - R_\oplus$). This can have an effect up to $0.7\,\mathrm{W\,m^{-2}}$.

For simplicity, the Earth-Sun system is rotated in a way that the simulation location (lat, long) is set to (0, 0) and the Sun is set along the equator towards the east (longitudinal) according to the solar zenith angle (SZA). Thus, the Sun will stand in zenith at (0, SZA). However, the SZA is defined at the simulation location at TOA and not at the Earth's centre. This is illustrated in Figure 5.1. There the SZA (θ) is larger than the longitude at which the Sun stands in zenith (φ). Thus φ must be greater than the SZA (up to 0.002°). Otherwise, the flux at TOA is smaller than the target. This leads to errors of

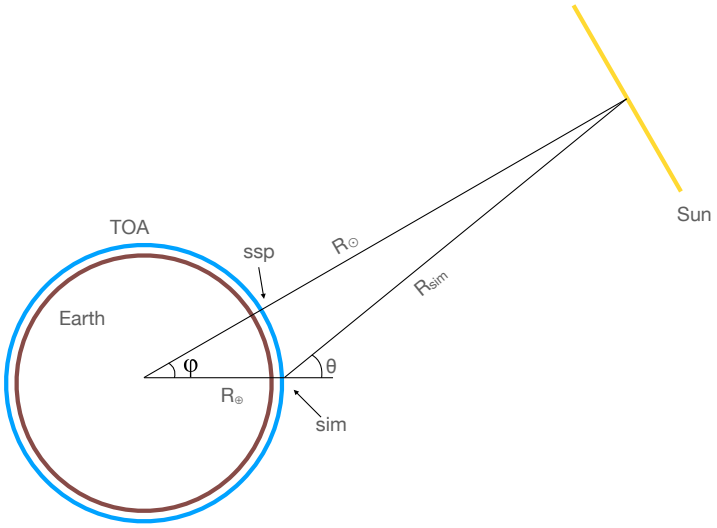

Figure 5.1: Illustration of the Geometry of Earth and Sun in ARTS. Shown are angles and distances between the centre of the Sun, the centre of the Earth and a simulation location.

about 0.1 W m^{-2}. This can be corrected according to the following:

$$\varphi = \theta - \arcsin\left(\frac{R_\oplus}{R_\odot}\sin(\pi - \theta)\right). \tag{5.1}$$

Both effects regarding the solar source could be neglected if the Sun was infinitely far away, which is obviously not the case, and thus this effect is non-negligible. The Sun is closer than you think. I want to emphasise that these corrections are made to accommodate the input from RFMIP, but these effects are physically correct and desired.

5.2 Results

As described above, it is vital that the incoming fluxes at TOA are accurate, as these are the driving force for all radiation in the shortwave regime.

Figure 5.2 shows the differences between LBLRTM, RRTMG and ARTS to the target TSI. As seen in Figure 4.8, the flux decreases cosinusoidally with the SZA. To compensate for this and gain comparability with the target TSI, the fluxes were scaled by the inverse of the cosine of the SZA. About half of the sites show no data points because the Sun is below the horizon for those sites and the flux is set to zero. Plane parallel models can not simulate this case. Optimising the `iyClearsky` solver for fluxes would allow us to also simulate fluxes for SZA greater than 90 °. Site 45 has an SZA of 87.6° and thus the sun is slightly above the horizon. However, LBLRTM presumably only simulates up to SZA around 87 degrees and therefore all fluxes for this site are set to zero and are also excluded from the analysis.

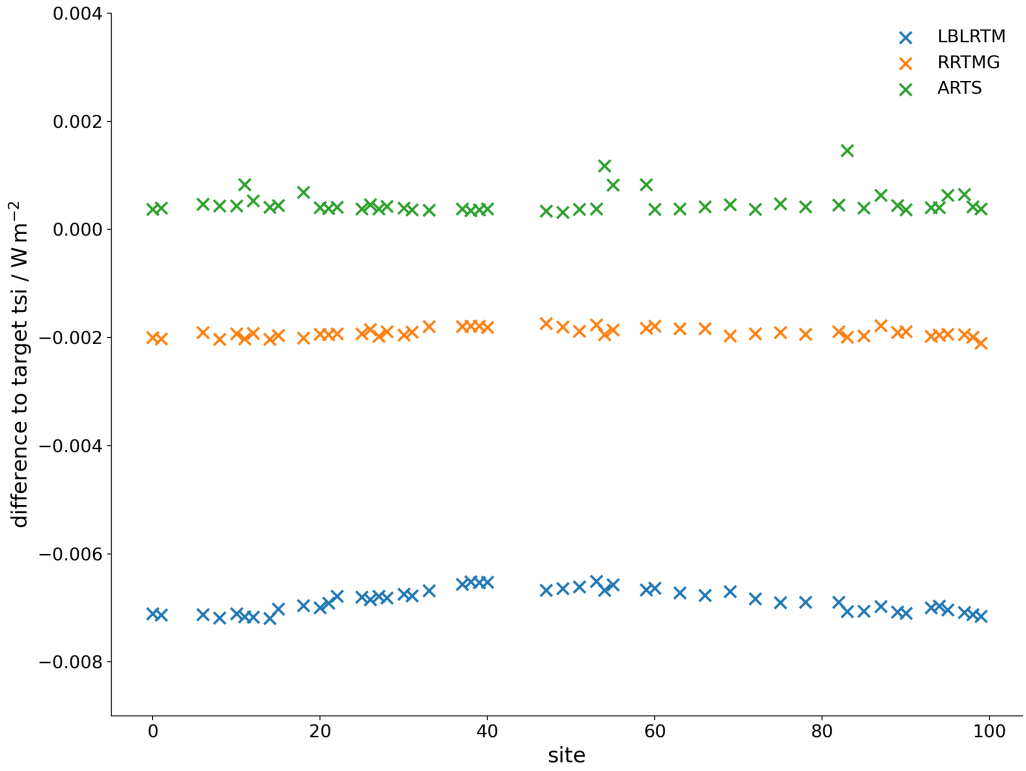

Figure 5.2: Difference of ARTS (green), RRTMG (orange), and LBLRTM (blue) to the target TSI for all sites with solar zenith angle less than 87 degrees. The flux of the simulation is scaled by the inverse of the cosine of the solar zenith angle.

LBLRTM has the largest offset to the target TSI with an average of 7 mW m^{-2}. I suspect that in LBLRTM, TOA is defined as 100 km above the surface and thus, the fluxes at the uppermost level (about 60 km) are underestimated. RRTMG underestimates the TSI by about 2 mW m^{-2} and ARTS overestimates slightly by 0.4 mW m^{-2}. For some sites, the flux differs significantly more from the target TSI than others. This is due to the high SZA at these sites. There the simulated fluxes are relatively small and scaling by the inverse of the cosine of the high SZA can lead to small numerical inaccuracies resulting in this offset.

In the left panel of Figure 5.3, the downward flux at the surface is shown. ARTS simulates slightly higher fluxes than LBLRTM (0.37 % on average). This corresponds to an absolute difference of 0.75 W m^{-2}. The standard deviation over all considered sites is 0.48 %, which corresponds to a spread of 0.40 W m^{-2}. RRTMG overestimates on average by 1.14 % (2.87 W m^{-2}), which is higher compared to ARTS and has a higher spread of 1.44 % (0.90 W m^{-2}). ARTS is thus almost a factor of 4 closer in absolute values to the simulated downward fluxes by LBLRTM than RRTMG. The great agreement between the two models is as expected, as both are more physically accurate line-by-line models and thus should be more precise.

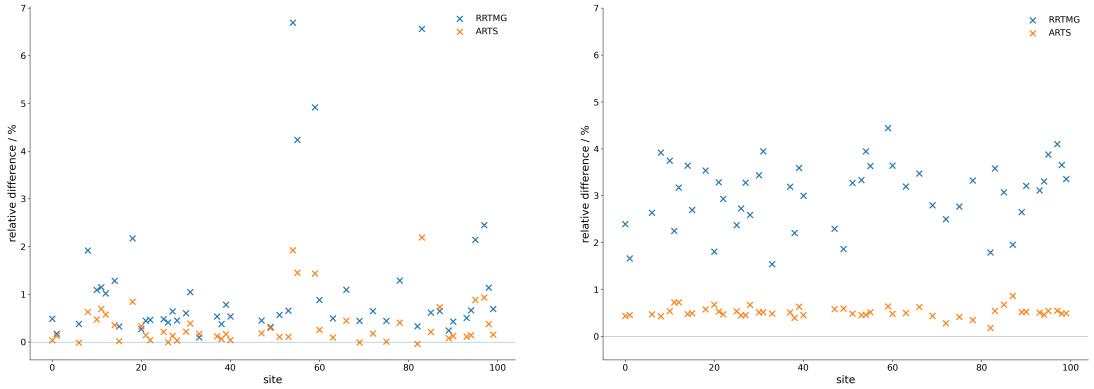

a) Downward flux at the surface.

b) Upward flux at the TOA.

Figure 5.3: Relative differences of downward fluxes at the surface (left) and upward fluxes at the TOA (right) simulated from ARTS (orange) and RRTMG (blue) to LBLRTM.

The relative error for the upward fluxes at the surface is identical to the downward flux, as the upward flux is just the reflection of the downward flux with the given respective albedo. The absolute value of the flux changes according to the albedo, but the relative difference stays the same.

The upward flux at the TOA, i.e. the outgoing shortwave radiation, can be seen in the right panel of Figure 5.3. There are higher differences in the upward flux at the TOA than in the downward fluxes at the surface with 0.52 %. However, due to the smaller absolute values in the upward fluxes, this corresponds to an absolute difference of 0.50 $\mathrm{W\,m^{-2}}$. The spread is small with a standard deviation of 0.11 % (0.36 $\mathrm{W\,m^{-2}}$). RRTMG has a larger deviation to LBLRTM than ARTS at all sites with an average difference of 3.04 % (2.55 $\mathrm{W\,m^{-2}}$) and a significantly higher spread of 0.69 % (0.86 $\mathrm{W\,m^{-2}}$). The upward fluxes at TOA look more like a systematic difference between ARTS and LBLRTM, but the downward fluxes show a strong dependence on the site. At some sites, the deviation is very small and at other sites, it is up to 2 %.

It was found that the differences highly depend on the length of the propagation path through the atmosphere. To quantify this length of the propagation path the parameter 'relative path length' (RPL) is introduced. It is the inverse of the cosine of the SZA. When the sun is at the zenith and shines directly onto the surface, the RPL has a value of 1. With a solar zenith angle of 60 degrees, the length of the path doubles and the RPL is 2. Thus, it is the effective number of atmospheres through which the radiation must propagate. For high SZA the RPL increases strongly.

The left panel in Figure 5.4 shows the dependencies of the relative difference between the models on the RPL. The differences between ARTS and LBLRTM increase linearly with the RPL as the strong agreement with the linear regression shows (RMSE=0.11). RRTMG does not show such a good linear relationship (RMSE=0.56) and the difference seems to increase more strongly towards high RPL.

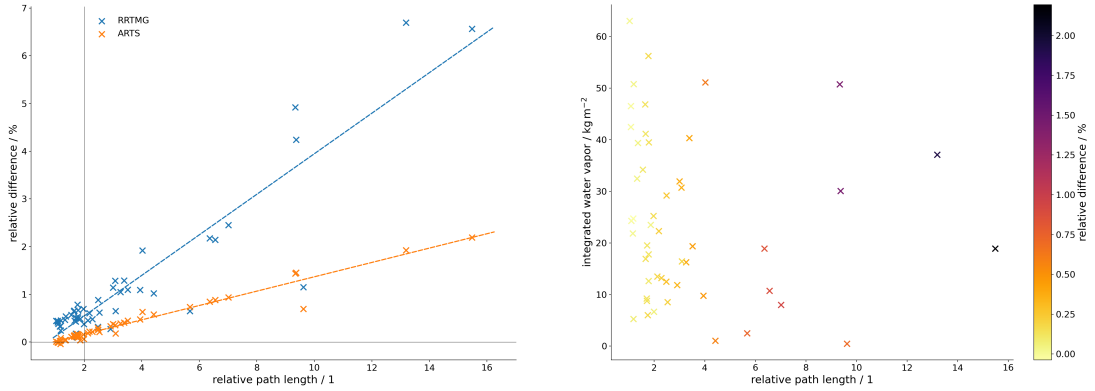

Figure 5.4: Relative differences of downward fluxes at the surface from ARTS (orange) and RRTMG (blue) to LBLRTM sorted by the relative path length (left panel). Linear regression for both models is shown as the dashed lines. The path length for a solar zenith angle of 60 degrees is highlighted with the black vertical line. The right panel shows the relative difference of downward fluxes at the surface simulated by ARTS and LBLRTM sorted by the relative path length and integrated water vapor.

Since the overestimation of the flux increases linearly with path length, it can be assumed that there is a small systematic difference in the extinction between the models, as slight differences in the physics between models can accumulate.

Since no spectral information is given in the reference data, no investigations of spectral dependency can be made. These could lead to some more precise information on where the differences between the models are. If these were given, one could compare various wavelengths, at which different absorbers are important to gain information about the impact of these absorbers. Alternatively, spectral fluxes in the atmospheric window in the visible band could be compared to investigate the agreement of the models for the Rayleigh scattering. However, since water vapor and ozone concentrations are varying at different sites. This could be used to compare, for example, the differences in flux at sites with high water vapor to sites with low water vapor. It is important that the RPL between these sites is comparable, to eliminate its influence. This analysis is done in the following.

In the right panel of Figure 5.4, the differences in the downward flux at the surface between ARTS and LBLRTM are shown, sorted by the RPL and the integrated water vapor. Integrated water vapor is a measure of how much water vapor is contained in the whole atmospheric column. Three sites have a comparable RPL of about 9.6 and one of the atmospheres (site 11) is extremely dry. This dryer site shows significantly smaller differences than the two moister sites. However, there is almost no difference between the moister sites, although they also have different integrated water vapor contents. Furthermore, this effect can not be seen in sites with shorter RPL, but this may be because the distance is too short to have a noticeable effect.

Figure 5.5 supports the hypothesis that differences in extinction are based on differ-

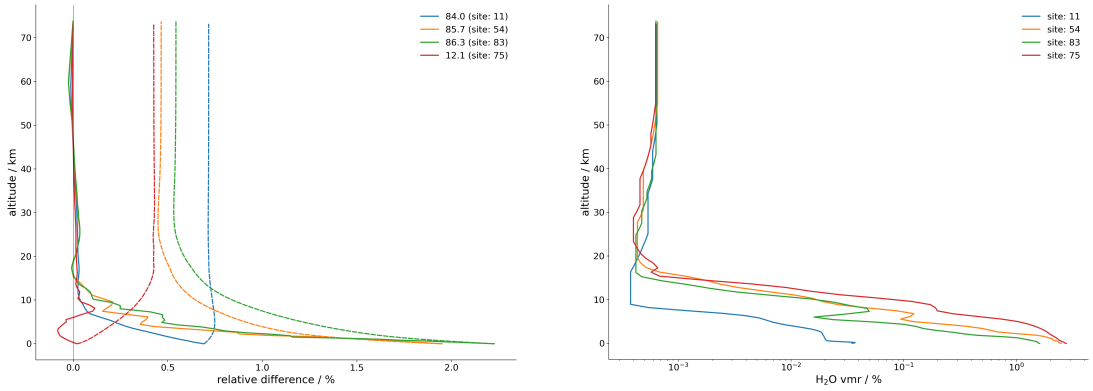

Figure 5.5: Profiles of the relative difference of ARTS to LBLRTM for up (dashed lines)- and downward (solid lines) fluxes for sites with solar zenith angles of 12.1, 84.0, 85.7, and 86.3 degrees (left panel) and their respective water vapor profiles (right panel).

ences in water vapor concentration. Profiles of the relative difference of ARTS to LBLRTM for the downward (solid lines) fluxes for sites with solar zenith angles of 84.0, 85.7, and 86.3 (and 12.1 as a reference) degrees and their respective water vapor (Volume Mixing Ratio - VMR) profiles are shown. It can be clearly seen, that site 11 is the driest, with the smallest water vapor VMR in the troposphere and the lowest tropopause with 10 km. For the sites with the large RPL (high SZA), the relative difference matches roughly the water vapor VMR profile, as the relative difference increases towards the surface starting at the height of the tropopause. The relative error of site 83 is slightly higher than site 54 even though slightly more water vapor is present. This is presumable due to the difference in RPL which has a larger effect on the relative difference as the effect of water vapor content. Therefore, I assume that the absorption by water vapour in ARTS is weaker than in LBLRTM and thus, the radiation is overestimated. There may be differences in the water vapour absorption, as for the reference simulations with LBLRTM, the MT_CKD continua version 3.2 was used and ARTS uses version 3.5. The same analysis was performed for ozone, but it was found that it has less to no impact on the differences between ARTS and LBLRTM. Thus, the integration of the ozone absorption cross sections (see Sec. 2.2.2) provides reliable and correct absorption coefficients. Differences in absorption of other species are unlikely, as both models utilize the HITRAN absorption database.

Therefore, it is assumed that the rest of the differences are mainly caused by different implementations of the Rayleigh scattering. I suggest that the Rayleigh scattering coefficient is on effectively slightly stronger. In Section 4.5 we saw that the upward flux is about constant as scattering and absorption are balancing each other. However, at site 75 (see Fig. 5.5 red line) the relative difference of the upward flux increases with height and converges toward a relative difference of about 0.5 % For sites 54 and 83 the relative difference is decreasing with height and converges towards the same relative difference. At site 11 the relative difference in the upward flux is almost constant with height as the relative difference is about 0.5 % at the surface. Because scattering is the only way to feed

the upward flux besides reflection at the surface, I suggest that the scattering coefficient is to high by about 0.5 %. Resulting in a systematic difference in the upward fluxes at TOA.

Moreover, there seems to be a difference in the models that leads to an underestimation of ARTS. This can be seen in the upper troposphere of site 75. This difference is unexplained.

Besides differences in the physics itself, differences can be introduced by varying approaches and philosophies in the model development. For example, in LBLRTM, the TSI is defined in 100 km (assumption) and not at the top model level as in ARTS and thus, the flux in the uppermost level is underestimated compared to the target TSI. A possible difference that would explain the dependence on the RPL is a difference in the refractive index. However, no further information on this could be found. Another difference is that in ARTS, all concentrations, as well as temperature and pressure, are expressed on levels and not on the layers, as it is the case in the given dataset. Furthermore, the specific settings used for the simulations have an impact. For instance, the frequency grid, as more or fewer absorption bands could be present, or the angular resolution on which the radiance is simulated and integrated to determine the fluxes. This is checked by running a high vertical resolution simulation using the given concentrations on the layers and the interpolation the levels. However, this has no significant influence as the differences changes by less than 0.1%. The same applies to the angular resolution. For this purpose, the number of streams (discrete ordinates) was adjusted in DISORT. RRTMG was fitted to results with DISORT simulations on 2 streams. However, the differences seem to result from the approximations introduced in RRTMG and not from the number of streams used in the reference simulations.

Overall the results show a great agreement with the LBLRTM model. The absolute difference in the downward flux is on average small with $0.75\,\mathrm{W\,m^{-2}}$. It was found that towards high solar zenith angles, the differences strongly increase linearly with the path through the atmosphere. If one restricts the simulations to the sites with an SZA below 60 degrees, the absolute difference in the downward flux at the surface is $0.48\,\mathrm{W\,m^{-2}}$ (0.08 %), although fluxes increase towards low SZA. The difference in upward fluxes would decrease to $0.53\,\mathrm{W\,m^{-2}}$. This restriction seems reasonable since the plane-parallel assumption becomes inaccurate at these SZA (see Sec. 4.2.1).

Pincus et al. [2020] compare radiative forcings of the six contributing line-by-line models against each other, as this is the important quantity for climate models. Their estimate of the radiative forcing is within $0.025\,\mathrm{W\,m^{-2}}$. The radiative forcing is defined as the change between present-day and preindustrial conditions in net downward flux at (TOA) and the surface. I suspect that ARTS lies within this range because in the calculation of the radiative forcing some of the above-listed effects acting on the differences

between the models are cancelling and effectively lowering the derivation. For example, I aspect that in preindustrial conditions the same dependence on the relative path as well as some systematic difference at TOA is present and close of similar magnitude as in the present day. Thus they will cancel out in the net fluxes leading to smaller differences.

6 Summary and Conclusion

This thesis aimed to make ARTS suitable for simulations in the shortwave regime. Thus, a solar source needed to be included. Of course, this requires a reference spectrum of a star or, in the case of this thesis, of the Sun. The May 2004 spectrum of the Solar Irradiance Climate Data Record [Coddington et al., 2015] was used. The main assumptions made for the ARTS internal `iyClearsky` solver are the collimated beam approximation and the single scattering approximation. DISORT is a well-known radiative transfer solver, which is also integrated into ARTS. To implement the solar source term, it is necessary to consider that the wavelength of the shortwave radiation is small enough to be scattered by the molecules in the atmosphere. This is called Rayleigh scattering, and for this purpose, the Rayleigh scattering coefficient and the Rayleigh scattering function were introduced in ARTS. In addition, HITRAN, the included line data catalogue, has no line data of ozone in shortwave. However, ozone plays a vital role in absorption in the ultraviolet and visible range. Therefore, measured ozone absorption cross-sections by Gorshelev et al. [2014] and Serdyuchenko et al. [2014] were used, and fitting parameters were calculated to match the ARTS internal format for absorption.

A comparison between the two solvers `iyClearsky` and DISORT shows that, on the one hand, the insufficiency of the assumption that only the direct downward beam is scattered, because it was found that the scattering of the direct radiation reflected from the surface should be taken into account. This otherwise produces errors of at least 30 % in the diffuse field, which accounts for 7.7 % of the total downward flux at the surface and a solar zenith angle of 0 degrees. On the other hand, the single scattering assumption becomes more inaccurate at high zenith angles at the surface. The error in the direct flux at a solar zenith angle of 0 degrees is 2.3 % and will increase to 14.4 % for a solar zenith angle of 60 degrees. The error in the diffuse downward flux is estimated to be in the order of 5 %. Moreover, `iyClearsky` is not optimized to calculate irradiances in the shortwave. Thus, DISORT is used for the simulation of fluxes.

The influence of the choice of the spectral grid was analyzed, and for simplicity, a spectral grid of 32,768 wavelengths ranging equally spaced from 115.5 to 9,999.5 nm was chosen. This cuts $0.8\,\mathrm{W\,m^{-2}}$ of the total energy density of the Sun, but it can be compensated by scaling the reference spectra, interpolated on the specific spectral grid of the simulation, to the targeted total solar irradiance.

The choice of the solar reference spectrum is important because it varies over time in an 11-year cycle. This is particularly important in the UV range. For the simulation, the spectrum of May 2004 was chosen because it describes an intermediate solar activity.

First simulations of shortwave fluxes in the tropical FASCOD atmosphere show that the downward diffuse flux is 75.5 W m^{-2} at the surface, which is 7.7 % of the direct flux of the Sun. The upward irradiance at the surface is 30 % of the total downward flux as the surface reflectivity is 0.3. In the diffuse upward field, scattering source and absorption sink are close to balance, and thus, the diffuse upward flux is constant with altitude. In the spectral irradiances, information about the strength of scattering as well as about absorption by specific species can be deduced. An analysis of the flux as a function of the solar zenith angle shows that at TOA, there is an exact cosine dependence since the projection of the radiation onto the surface element of the flux definition has this cosine dependence precisely. At ground level, the irradiance at large solar zenith angles is smaller than the cosine dependence would determine. This is due to the longer path through the atmosphere.

To gain deeper insights into shortwave flux simulations, ARTS simulations of the RFMIP 'present-day' experiment are compared to LBLRTM and RRTMG. The aim was to identify possible weaknesses of ARTS. Generally, it was found that ARTS agrees better with the physically more accurate LBLRTM model than RRTMG, which is based on parametrizations and optimized for efficiency and speed. At TOA, ARTS represents the target total solar irradiance the best, with an average accuracy of $+0.4$ mW m^{-2}. To achieve this, adjustments for the spectrum's scaling factor and the Sun's position are needed. This is necessary due to the 3D nature of ARTS. The flux is correctly determined with respect to the inputs in ARTS. However, the information given by RFMIP is more suitable for plane-parallel models.

The difference between ARTS and LBLRTM is 0.75 ± 0.40 W m^{-2} in downward flux at the surface and 0.50 ± 0.36 W m^{-2} in upward flux at TOA. The differences between ARTS and LBLRTM were found to increase linearly with the effective path length through the atmosphere. I hypothesize that the differences are, on the one hand, caused by a weaker water vapor absorption caused by different continuum versions used in the models. On the other hand, the Rayleigh scattering coefficient is considerably larger in ARTS, resulting in stronger scattering compared to LBLRTM. This is attributed to the systematic relative difference of 0.5 % of the outgoing shortwave flux. The absorption by the newly integrated ozone absorption cross-sections is consistent with the absorption in LBLRTM.

Pincus et al. [2020] compare radiative forcings of six line-by-line models. Their estimate of the radiative forcing is within 0.025 W m^{-2}. I suspect ARTS to lie within that range, assuming that the dependence on the relative path and the systematic difference at TOA are of similar magnitude in the preindustrial and the present-day conditions. In that case, they will cancel out in the calculation of the radiative forcing. This would lead to smaller differences and result in a great agreement of ARTS with other state-of-the-art line-by-line models.

7 Outlook

The main issue to be addressed is the scattering of the reflected direct beam on the surface. This would drastically reduce the error in the diffuse field depending on the albedo. Furthermore, `iyClearsky` could be optimised for fluxes by calculating the flux from the smooth diffuse and the spiky direct beam separately and adding them afterwards. This can be addressed relatively easily to create better comparability and, at the same time, eliminate a significant error. Introducing higher scattering orders will be more complex and complicated.

Since an overestimation of the Rayleigh scattering coefficient is suspected, it might be worthwhile to include a more accurate model. It was suggested that the refractive index might have an influence. This is not possible to test further for DISORT, but a model of the shortwave could be introduced for the propagation path calculation in ARTS (instead of using the geometric path).

Spectral resolution simulations with LBLRTM could be done to identify further and improve ARTS's potential weaknesses.

8 Appendix

8.1 Stars in ARTS

This section briefly describes how we implemented and designed stars in ARTS. Generally, there can be multiple stars in ARTS with their individual spectra. As a spectrum, each star can be defined as a theoretical Planck Body with an effective emission temperature or with a user-defined spectrum. The spectra should be given at the photosphere of the star is chose because it is the most flexible for simulations with multiple stars or different positions of the star and planet. Since the input radiation at the TOA of the planet is directly calculated from the transfer of each star. This is done by

$$F_{\odot,TOA} = F_{\odot}\, sin^2(\alpha) \tag{8.1}$$

where $F_{\odot}$ is the spectrum at the star's photosphere and $\alpha = tan^{-1}(r_{\odot}/R_{\odot})$ is the angular radius of the star with radius $r_{\odot}$ m and a distance between the centre of the planet and the star $R_{\odot}$. Thus, in addition to the spectra of the star, the radius and distance must be given by the user. Defaults for this are reference values of our Sun ($r_{\odot} = 6.96342 \cdot 10^8$ m) and the astronomical unit as the distance $R_{\odot} = 1\, au = 1.495978707 \cdot 10^{11}$ m. Since for the calculations it is assumed that the stars are a point source with finite extent or that their rays are parallel to each other (collimated beam approximation), no limb effects of stars are included. Thus, stars in ARTS are effectively disks with finite radius $r_{\odot}$. The location of the star is specified as the location (ϑ, φ) at which the star stands in zenith. Since the position of the sun has a zenith and azimuth component, one is forced to perform the simulation in 3D, as ARTS only supports azimuthal dependencies in this geometry. In addition, a temperature can be specified. In the case of a black body star, this temperature is the emission temperature which defines the whole spectrum. In case the star spectrum is given this indicates the padding if the spectral grid of the simulation is outside the star spectrum data. One can choose -1 for zero padding at the edges or an effective temperature for padding using plack's law. For wavelength within the data, the star spectrum is linearly interpolated onto the simulation spectral grid.

Since most of the ARTS simulations and especially all simulations of this thesis refer to the Earth's atmosphere and thus, the star is the Sun, and realistic reference spectra are needed. For this, solar reference spectra as described in Section 2.2.1 are used. These are

converted to ARTS internal units and inversely scaled according to Equation 8.1 to the flux at the centre of the star. However, the distance used is not 1 au, but the distance between the stars and the subsolar point with a TOA altitude of 100 km ($R_\odot - r_\oplus - 100\,km$, with $r_\oplus$ being the radius of the Earth). This means that simulations at this location exactly reproduce the solar constant of the given spectra. All reference spectra (see Sec. 2.2.1) are processed this way and are included in the ARTS XML Data package [artsxml].

In the future, stars can also be specified via a local (measured) star spectrum at the simulation location as well as the local solar angles for the star's positions. This eliminates the need for the corrections described in Section 5.1.

8.2 Usage in ARTS

In this section, we will show how to perform ARTS simulation in the shortwave regime and which additional steps are needed to incorporate a star into a previous simulation in the longwave regime. For this demonstration, the pyarts package [pyarts] is used. Note that this is not a whole script for an ARTS simulation by rather which steps should be taken to incorporate a star in an existing run script.

First, simulations with a stellar source need a 3D atmosphere (not true for DISORT as a solver). This is done by calling:

```
1 ws.AtmosphereSet3D()
```

ARTS will ensure that all positions and line-of-sights of the sensor as well as the atmospheric conditions are set accordingly.

Since no refractive index has yet been implied for the shortwave, the propagation paths are simulated along the line of sight. This is done by setting the ppath step agenda to the geometric path:

```
1 ws.ppath_step_agendaSet(option="GeometricPath")
```

This does not need to be set for simulation with DISORT, as it determines the propagation paths itself.

For all simulations in the visible range, gas scattering should be considered and the Rayleigh scattering coefficient as well as the Rayleigh scattering matrix should be set. This is done via the gas scattering agenda:

```
1 ws.gas_scattering_agenda = gas_scattering_agenda__Rayleigh
2 ws.gas_scattering_do = 1
3 # gas scattering agenda
4 @pyarts.workspace.arts_agenda
5 def gas_scattering_agenda__Rayleigh(ws):
6     ws.Ignore(ws.rtp_vmr)
7     ws.gas_scattering_coefAirSimple()
8     ws.gas_scattering_matRayleigh()
```

This must also be set for simulation with DISORT, as information about the scattering properties is being passed.

For simulations with `iyClearsky`, the surface reflection type must be specified. Options are a Lambertian surface which is suitable for example for a desert (which is also used in DISORT), a specular reflection as it is the case on a smooth water surface or a Fresnel surface which represents a wavy ocean. These can be set with the help of the iy surface agenda.

```
ws.iy_surface_agenda = iy_surface_agenda__Lambertian

## surface scattering agenda
# lambertian surface
@pyarts.workspace.arts_agenda
def iy_surface_agenda__Lambertian(ws):
    ws.iySurfaceInit()
    ws.Ignore(ws.dsurface_rmatrix_dx)
    ws.Ignore(ws.dsurface_emission_dx)

    ws.iySurfaceLambertian()
    ws.iySurfaceLambertianDirect()


# specular surface
@pyarts.workspace.arts_agenda
def iy_surface_agenda__FlatReflectivity(ws):
    ws.iySurfaceInit()
    ws.Ignore(ws.dsurface_rmatrix_dx)
    ws.Ignore(ws.dsurface_emission_dx)

    ws.iySurfaceFlatReflectivity()
    ws.iySurfaceFlatReflectivityDirect()


# fresnel surface
@pyarts.workspace.arts_agenda
def iy_surface_agenda__FlatFresnel(ws):
    ws.iySurfaceInit()
    ws.Ignore(ws.dsurface_rmatrix_dx)
    ws.Ignore(ws.dsurface_emission_dx)

    ws.iySurfaceFlatRefractiveIndex()
    ws.iySurfaceFlatRefractiveIndexDirect()
```

Of course, the star itself still needs to be added. In this example, two stars are initialised. The first is instantiated with the solar reference spectrum from artsxml. It defaults to a distance of 1 au and the Sun's radius. Thus, the set star is the Sun over the location (`sun_latitude` , `sun_longitude`). The second star is instantiated by a user-defined solar spectrum measured at the location (`location_lat` , `location_lon` , `location_alt`). The star is at the local coordinates of (`sun_zenith` , `sun_azimuth`) and has the same radius as the Sun but is twice as far away.

```
gf2 = pyarts.xml.load('path/to/arts-xml-data/star/Sun/solar_spectrum_May_2004.xml')
# star spectrum at the star surface
ws.starsAddSingleFromGrid(
    star_spectrum_raw=gf2,
    latitude=sun_latitude,
    longitude=sun_longitude,
)

# star spectrum at the sim location
sun_distance = ws.stars.value[0].distance
ws.starsAddSingleFromGridAtLocation(
    star_spectrum_raw=ref_spec_at_location,
    distance=2*sun_distance,
    zenith=sun_zenith,
    azimuth=sun_azimuth,
    location_latitude=location_lat,
    location_longitude=location_lon,
    location_altitude=location_alt,
)
```

To perform the simulation, one of the following routines can be executed. A flux simulation can best be carried out with DISORT and the `DisortCalcIrradiance` method. Radiance simulations can be performed with DISORT and the `DisortCalcClearsky` method or with `iyClearsky`. For simulation with `iyClearsky`, the `iy_main_agenda` is defined as shown in the example, and `yCalc` performs the simulation.

```
## irradiances
ws.DisortCalcIrradiance()

## radiances
# DISORT
ws.DisortCalcClearsky()

# iyClearSky
ws.iy_main_agenda = iy_main_agenda__ClearSky
@pyarts.workspace.arts_agenda
def iy_main_agenda__ClearSky(ws):
    ws.ppathCalc()
    ws.iyClearsky()

ws.yCalc()
```

For more details see artsdocs. Happy simulating in the shortwave regime!

8.3 Surfaces

This section compares the Lambertian surface to a surface with specular reflection and the resulting upward flux, respectively. At the surface, the upward (denoted with a +-

superscript) flux is the integral over the downward-facing hemisphere of the bidirectional reflectance distribution function ρ, or BRDF, describes the angular distribution of the reflected radiation and the downward flux F^-.

$$F^+ = \int_0^{2\pi} \int_{2\pi}^{\pi} \rho(\nu, \vartheta, \varphi, \vartheta', \varphi')\ F^-\ cos\vartheta'\ sin\vartheta'\ d\vartheta'\ d\varphi', \tag{8.2}$$

where $'$ denotes the reflected radiation. For Lambertian surfaces, the radiation is independent of the direction of incidence and observation and for ARTS simulation even of frequency. Thus

$$\rho_{lam}(\nu, \vartheta, \varphi, \vartheta', \varphi') = \rho_{lam} = r/\pi, \tag{8.3}$$

where r is the reflectivity or $1 - \alpha$ with the albedo α of the surface [Thomas and Stamnes, 2002]. The downward flux is only dependent on the solar zenith angle $\vartheta_\odot$ and the reflection at the surface is assumed to be the first-order scattering event. Thus, reflection is only dependent on the direct beam and not the diffuse field. This yields:

$$F^+_{lam} = r\ F_\odot\ cos\vartheta_\odot. \tag{8.4}$$

For the mirror-like specular reflection, the incident beam is reflected directly so that the angle of reflection to the surface normal is equal to the angle of incidence to the surface normal. In the azimuthal component, the radiation is reflected in the opposing direction (180°). Therefore, the upward irradiance is

$$I^+_{spec} = r\ F_\odot\ \delta(cos\vartheta - cos\vartheta_\odot)\ \delta(cos\varphi - [cos\varphi_\odot + \pi]. \tag{8.5}$$

Integration over the downward-facing hemisphere yields that the upward flux F^+_{spec} equals F^+_{lam}. This is also to be expected, as energy conservation still holds. Therefore, the surface type does not influence the simulated fluxes.

8.4 Species in RFMIP

List of all species contained in RFMIP:

- oxygen - O_2, nitrogen - N_2
- water vapor - H_2O
- ozone - O_3
- methane CH_4
- carbon monoxide - CO, carbon dioxide - CO_2
- methyl bromide - CH_3Br, methyl chloride - CH_3Cl

- nitrogen trifluoride - NF_3, nitrous oxide - NO
- SF_6
- SO_2F_2
- CH_2Cl_2
- CH_3CCl_3
- HCFC141, HCFC142
- CFC113-115, CFC11, CFC12
- halon1211, halon1301, halon2402
- carbon tetrachloride - CCl_4, carbon tetraflorid - CF_4
- C_iF_{2i+2} with $i \in 2, 3, 4, 5, 6, 8$ ($i = 7$ not included)
- Chlorodifluoromethane - HCFC22, HFC125, HFC134, HFC143, HFC152, HFC227, HFC236 (not included), HFC23, HFC245 (not included), HFC32, HFC4310 (not included)

List of Figures

Bibliography

SA Buehler, Patrick Eriksson, Thomas Kuhn, A Von Engeln, and C Verdes. Arts, the atmospheric radiative transfer simulator. *Journal of Quantitative Spectroscopy and Radiative Transfer*, 91(1):65–93, 2005.

Patrick Eriksson, SA Buehler, CP Davis, C Emde, and Oliver Lemke. Arts, the atmospheric radiative transfer simulator, version 2. *Journal of Quantitative Spectroscopy and Radiative Transfer*, 112(10):1551–1558, 2011.

artswebpage. *ARTS* the atmospheric radiative transfer simulator. URL https://radiativetransfer.org.

Lukas Kluft, Manfred Brath, Stefan A Buehler, and Bjorn Stevens. Cloud-altitude feedbacks in the 1d-rce model konrad. *Lukas Kluft*, page 71, 2020.

Karl E Taylor, Ronald J Stouffer, and Gerald A Meehl. An overview of cmip5 and the experiment design. *Bulletin of the American meteorological Society*, 93(4):485–498, 2012.

John Theodore Houghton, Geoffrey J Jenkins, and Jim J Ephraums. Climate change: the ipcc scientific assessment. *American Scientist;(United States)*, 80(6), 1990.

Robert Pincus, Eli J Mlawer, Lazaros Oreopoulos, Andrew S Ackerman, Sunghye Baek, Manfred Brath, Stefan A Buehler, Karen E Cady-Pereira, Jason NS Cole, Jean-Louis Dufresne, et al. Radiative flux and forcing parameterization error in aerosol-free clear skies. *Geophysical Research Letters*, 42(13):5485–5492, 2015.

Robert Pincus, Piers M Forster, and Bjorn Stevens. The radiative forcing model intercomparison project (rfmip): experimental protocol for cmip6. *Geoscientific Model Development*, 9(9):3447–3460, 2016.

Knut Stamnes, Si-Chee Tsay, Warren Wiscombe, and Istvan Laszlo. Disort, a general-purpose fortran program for discrete-ordinate-method radiative transfer in scattering and emitting layered media: documentation of methodology. 2000.

Odele Coddington, J Lean, Doug Lindholm, Peter Pilewskie, and Martin Snow. Program: Noaa climate data record (cdr) of solar spectral irradiance (ssi), version 2.1 noaa national centers for environmental information, 2015.

O Coddington, JL Lean, P Pilewskie, M Snow, and D Lindholm. A solar irradiance climate data record. *Bulletin of the American Meteorological Society*, 97(7):1265–1282, 2016. doi: 10.1175/BAMS-D-14-00265.1.

artscat. Arts developers - arts cat data. URL https://www.radiativetransfer.org/tools/#arts-cat-data.

Laurence S Rothman, André Barbe, D Chris Benner, LR Brown, Claude Camy-Peyret, MR Carleer, K Chance, Cathy Clerbaux, Victor Dana, V Malathy Devi, et al. The hitran molecular spectroscopic database: edition of 2000 including updates through 2001. *Journal of Quantitative Spectroscopy and Radiative Transfer*, 82(1-4):5–44, 2003.

Victor Gorshelev, Anna Serdyuchenko, Mark Weber, W Chehade, and JP Burrows. High spectral resolution ozone absorption cross-sections–part 1: Measurements, data analysis and comparison with previous measurements around 293 k. *Atmospheric Measurement Techniques*, 7(2):609–624, 2014.

A Serdyuchenko, V Gorshelev, M Weber, W Chehade, and JP Burrows. High spectral resolution ozone absorption cross-sections–part 2: Temperature dependence. *Atmospheric Measurement Techniques*, 7(2):625–636, 2014.

artsxml. Arts developers - arts xml data. URL https://www.radiativetransfer.org/tools/#arts-xml-data.

Gail P Anderson, Shepard Anthony Clough, FX Kneizys, James H Chetwynd, and Eric P Shettle. Afgl atmospheric constituent profiles (0.120 km). Technical report, Air Force Geophysics Lab Hanscom AFB MA, 1986.

Robert Pincus, Stefan A Buehler, Manfred Brath, Cyril Crevoisier, Omar Jamil, K Franklin Evans, James Manners, Raymond L Menzel, Eli J Mlawer, David Paynter, et al. Benchmark calculations of radiative forcing by greenhouse gases. *Journal of Geophysical Research: Atmospheres*, 125(23):e2020JD033483, 2020.

SA Clough, MW Shephard, EJ Mlawer, JS Delamere, MJ Iacono, K Cady-Pereira, S Boukabara, and PD Brown. Atmospheric radiative transfer modeling: A summary of the aer codes. *Journal of Quantitative Spectroscopy and Radiative Transfer*, 91(2):233–244, 2005.

Eli J Mlawer, Steven J Taubman, Patrick D Brown, Michael J Iacono, and Shepard A Clough. Radiative transfer for inhomogeneous atmospheres: Rrtm, a validated correlated-k model for the longwave. *Journal of Geophysical Research: Atmospheres*, 102 (D14):16663–16682, 1997.

Gary E Thomas and Knut Stamnes. *Radiative transfer in the atmosphere and ocean*. Cambridge University Press, 2002. doi: \url{https://doi.org/10.1017/9781316148549.7,13,14}.

Kuo-Nan Liou. *An introduction to atmospheric radiation*, volume 84. Elsevier, 2002a.

Ilias M Vardavas, Ilias Vardavas, and Frederic Taylor. *Radiation and Climate: Atmospheric energy budget from satellite remote sensing*, volume 138. Oxford University Press, 2011.

Stefan Alexander Buehler, Manfred Brath, Oliver Lemke, Øivind Hodnebrog, Robert Pincus, Patrick Eriksson, Iouli Gordon, and Richard Larsson. A new halocarbon absorption model based on hitran cross-section data and new estimates of halocarbon instantaneous clear-sky radiative forcing. *Earth and Space Science Open Archive*, page 31, 2022. doi: 10.1002/essoar.10511615.1. URL https://doi.org/10.1002/essoar.10511615.1.

Grant W. Petty. *A first course in atmospheric radiation*. Sundog Publ., 2. ed. edition, 2006.

DR Bates. Rayleigh scattering by air. *Planetary and Space Science*, 32(6):785–790, 1984. doi: \url{https://www.sciencedirect.com/science/article/pii/0032063384901028}.

Kuo-Nan Liou. *An introduction to atmospheric radiation*, volume 84. Elsevier, 2002b.

Michael I Mishchenko, Larry D Travis, and Andrew A Lacis. *Scattering, absorption, and emission of light by small particles*. Cambridge university press, 2002.

Subrahmanyan Chandrasekhar. *Radiative transfer*. Courier Corporation, 2013.

Eli J Mlawer, Vivienne H Payne, Jean-Luc Moncet, Jennifer S Delamere, Matthew J Alvarado, and David C Tobin. Development and recent evaluation of the mt_ckd model of continuum absorption. *Philosophical Transactions of the Royal Society A: Mathematical, Physical and Engineering Sciences*, 370(1968):2520–2556, 2012.

DJ Paynter and V Ramaswamy. An assessment of recent water vapor continuum measurements upon longwave and shortwave radiative transfer. *Journal of Geophysical Research: Atmospheres*, 116(D20), 2011.

Cyril Richard, Iouli E Gordon, Laurence S Rothman, Martin Abel, Lothar Frommhold, Magnus Gustafsson, J-M Hartmann, Christian Hermans, Walter J Lafferty, Glenn S Orton, et al. New section of the hitran database: Collision-induced absorption (cia). *Journal of Quantitative Spectroscopy and Radiative Transfer*, 113(11):1276–1285, 2012.

Arne Dahlback and Knut Stamnes. A new spherical model for computing the radiation field available for photolysis and heating at twilight. *Planetary and Space Science*, 39(5): 671–683, 1991.

libradtran. *libradtran.org (Plane-parallel versus pseudo-spherical versus spherical)*. http://www.libradtran.org/doku.php?id=user_area:plane-parellel_versus_pseudo-spherical_versus_spherical. Accessed: 2022-10-04.

SA Buehler, A Von Engeln, E Brocard, Viju Oommen John, Thomas Kuhn, and Patrick Eriksson. Recent developments in the line-by-line modeling of outgoing longwave radiation. *Journal of Quantitative Spectroscopy and Radiative Transfer*, 98(3):446–457, 2006.

John P. Burrows, Peter Borrell, and Ulrich Platt. *The Remote Sensing of Tropospheric Composition from Space*. Physics of Earth and Space Environments. Springer-Verlag Berlin Heidelberg, 2011. URL https://dx.doi.org/10.1007/978-3-642-14791-3.

NOAA. SPACE WEATHER PREDICTION CENTER solar cycle progression. URL https://www.swpc.noaa.gov/products/solar-cycle-progression.

open API. Open elevation public api. URL (https://open-elevation.com).

pyarts. Arts developers - pyarts. https://atmtools.github.io/arts-docs-master/pyarts/index.html. Accessed: 2022-12-07.

artsdocs. Arts developers - arts built-in documentation server. https://atmtools.github.io/arts-docs-master/docserver/index.html. Accessed: 2022-12-07.

Acknowledgement

First of all, I would like to thank Prof. Dr. Stefan Bühler for being my primary supervisor, who offered me the excellent opportunity to write my thesis in his research group. In fact, ARTS is the model he started to develop for his diploma, and now I am developing it further in a similar context. He guided me on my journey and nudged me in the right direction if I got lost.

Secondly, I want to thank my second supervisor Manfred Brath, who helped a lot in developing the principles and ideas for the implementation in ARTS. He did most of the heavy lifting to incorporate my developed methods into the workflow of ARTS, which otherwise would have been overwhelming. Freddy always had an open ear and never got tired of explaining the theoretical background to me, but he still made it possible for this thesis to be my own work.

Furthermore, I would like to thank Oliver Lemke. He always had 'a second' for me to all computer-related questions or chat about the latest things from the world of programming. Together with Richard, he taught me a lot about programming.

Most of the time, I shared my office with Conni and Flo. Together with Marc, they made the time spent in the office enjoyable, were always there for topic-related discussions, and provided new motivation with, for example, the "Franzbrötchen" bet.

All of the above are part of the working group 'Climate, Radiation, Remote Sensing' and have provided a comfortable yet motivating working atmosphere.

Finally, I must express my thankfulness to my parents, Helke Stammerjohann and Dirk Petersen, my family and all my friends, without whose support throughout the writing process and the whole time of my studies would not have been so much fun or even possible.

Special thanks to Flo and Matthias, who reviewed the main parts of this thesis and gave me a new approach if I got stuck with writing and have thus made a contribution to this thesis. Additionally, I would like to thank my girlfriend Leonie and everybody else who came to my office to motivate me even in more challenging times or forced me to take a short break and get back to work refreshed.

Eidesstattliche Versicherung

Hiermit versichere ich an Eides statt, dass ich die vorliegende Arbeit im Studiengang M.Sc. Meteorologie selbstständig verfasst und keine anderen als die angegebenen Hilfsmittel – insbesondere keine im Quellenverzeichnis nicht benannten Internet-Quellen – benutzt habe. Alle Stellen, die wörtlich oder sinngemäß aus Veröffentlichungen entnommen wurden, sind als solche kenntlich gemacht. Ich versichere weiterhin, dass ich die Arbeit vorher nicht in einem anderen Prüfungsverfahren eingereicht habe und die eingereichte schriftliche Fassung der auf dem elektronischen Speichermedium entspricht.
Ich bin mit einer Einstellung in den Bestand der Bibliothek des Fachbereiches einverstanden.

Hamburg, den _____ Unterschrift: _____